Title

In vivo optogenetic manipulations of endogenous proteins reveal spatiotemporal roles of microtubule and kinesin in dendrite patterning.

Journal

Science Advances, 10(35)

Authors

Xu, Yineng

Wang, Bei

Bush, Inle

et al.

Publication Date

2024-08-30

DOI

10.1126/sciadv.adp0138

CELLULAR NEUROSCIENCE

In vivo optogenetic manipulations of endogenous proteins reveal spatiotemporal roles of microtubule and kinesin in dendrite patterning

Yineng Xu[1], Bei Wang[1], Inle Bush[1], Harriet AJ Saunders[2], Jill Wildonger[2,3], Chun Han[1]*

During animal development, the spatiotemporal properties of molecular events largely determine the biological outcomes. Conventional gene analysis methods lack the spatiotemporal resolution for precise dissection of developmental mechanisms. Although optogenetic tools exist for manipulating designer proteins in cultured cells, few have been successfully applied to endogenous proteins in live animals. Here, we report OptoTrap, a light-inducible clustering system for manipulating endogenous proteins of diverse sizes, subcellular locations, and functions in *Drosophila*. This system turns on fast, is reversible in minutes or hours, and contains variants optimized for neurons and epithelial cells. By using OptoTrap to disrupt microtubules and inhibit kinesin-1 in neurons, we show that microtubules support the growth of highly dynamic dendrites and that kinesin-1 is required for patterning of low- and high-order dendritic branches in differential spatiotemporal domains. OptoTrap allows for precise manipulation of endogenous proteins in a spatiotemporal manner and thus holds promise for studying developmental mechanisms in a wide range of cell types and developmental stages.

INTRODUCTION

Animal development involves a myriad of molecular events that occur at specific times and locations. The same molecular event can result in vastly different outcomes depending on the spatiotemporal properties of the biological context. Spatiotemporal regulation is particularly important for the development of neurons: Spatially, neurons can span broad domains and receive distinct signaling inputs at different compartments because of unique interactions with the surrounding microenvironment. Temporally, neurons undergo distinct stages of differentiation, including neuronal migration, axon pathfinding, dendrite arborization, and synapse formation, before forming functional circuits. Thus, a deeper understanding of the assembly of the nervous system requires effective approaches to probe the spatiotemporal properties of molecular events in neurons.

However, traditional loss-of-function (LOF) approaches, such as gene mutation and RNA interference (RNAi), and gain-of-function (GOF) approaches, such as gene overexpression (OE), are insufficient for extracting fine spatiotemporal information because they typically affect the entire cell for a long duration. This caveat is particularly limiting for studying proteins that play multiple roles in different parts of the cell or at different stages of differentiation. An example is the microtubule (MT) cytoskeleton, which provides mechanical support to neuronal branches and serves as a track for motor-based cargo transport (*1*, *2*). MT assembly, organization, and dynamics are important for dendrite growth and maintenance (*3*), and MT-based motors, including kinesin and dynein, are important for neuronal polarity and dendrite patterning (*4*). However, how MTs and MT-based motors control specific aspects of dendrite morphogenesis, such as arbor size and location of dynamic branches, at different stages of neuronal development in vivo remains poorly understood. While optogenetic techniques to regulate MTs and motors are being developed (*5*–*9*), it remains a challenge to manipulate MTs and their motors in neurons inside animals with high spatiotemporal precision.

In recent years, optogenetics has emerged as a powerful approach for finely dissecting cellular mechanisms. Taking advantage of protein modules that change confirmations or binding affinities upon activation by light of specific wavelengths, light-controllable agents have been developed to produce specific signaling outputs (*10*–*13*). Light-mediated manipulation of protein activity has been achieved through a variety of mechanisms, including but not limited to protein uncaging (*14*–*16*), protein dimerization/oligomerization (*17*–*19*), trapping of proteins inside large complexes (*20*, *21*), reconstitution of split proteins (*22*–*24*), relocating proteins to the plasma membrane (*25*, *26*), and recruitment of effectors to specific genetic loci (*27*). These tools offer an unprecedented level of control and specificity, allowing for precise and instantaneous manipulation of molecular events in cells.

Optogenetic approaches hold great promise also for in vivo study of developmental mechanisms. Several optogenetic tools originally developed for cultured cells have been successfully applied to ex vivo tissues and developing embryos, leading to novel insights into collective cell migration (*28*), embryonic patterning (*29*–*32*), axon guidance (*33*, *34*), and acting cytoskeleton regulation (*35*). However, the application of optogenetics in vivo has been limited by several factors. First, most existing optogenetic tools can only manipulate specific designer proteins and require their OE to produce dominant-active effects. Thus, it has been difficult to apply a single optogenetic system to manipulate a wide range of endogenous proteins that are regulated by diverse mechanisms. Furthermore, cells inside animals exhibit diverse morphologies and interact with complex microenvironments; a single-tool design may not be effective in all cell types. Last, because it is challenging to maintain controlled lighting on the target cells inside behaving animals, optogenetic applications in whole organisms over extended developmental periods have been rare.

[1]Weill Institute for Cell and Molecular Biology, Department of Molecular Biology and Genetics, Cornell University, Ithaca, NY 14853, USA. [2]Department of Biochemistry, University of Wisconsin-Madison, 440 Henry Mall, Madison, WI 53706, USA. [3]Pediatrics Department and Biological Sciences Division, Section of Cell and Developmental Biology, University of California San Diego, 9500 Gilman Drive, La Jolla, CA 92093, USA.
*Corresponding author. Email: chun.han@cornell.edu

To overcome these difficulties, we developed OptoTrap, a versatile optogenetic system in *Drosophila* that allows in vivo manipulation of endogenous proteins that are tagged with a green fluorescent protein (GFP) or a split GFP fragment. This system acts through light-induced clustering/aggregation of the protein of interest (POI) and can be used to probe spatiotemporal roles of a wide range of proteins in specific cell types. By engineering variants that exhibit different kinetics and oligomerization properties, we identified ones that can efficiently and reversibly cluster proteins in epithelial cells and neurons. These tools allowed us to manipulate protein activities in both cell types over several days during *Drosophila* larval development. To understand how MTs and their associated motors control dendrite patterning, we used OptoTrap to manipulate α-tubulin and kinesin-1 in *Drosophila* class IV dendritic arborization (C4da) neurons, somatosensory neurons that elaborate complex dendritic arbors on the larval epidermis (*36*). Our investigation reveals the critical role of MTs in maintaining the growth dynamics of terminal dendrites and differential temporal requirements of kinesin-1 in the patterning of low- and high-order dendritic branches.

RESULTS

The OptoTrap system builds on blue light–sensitive protein modules

To induce protein aggregation by light, we designed an OptoTrap (for optogenetic trapping) system that is built upon two blue light–activatable modules, CRY2olig and Magnets. CRY2olig (*37*), a mutant version of the *Arabidopsis* cryptochrome 2 (CRY2) (*38*), exhibits a great ability to cluster upon blue light stimulation. Magnets consist of a positive magnet (pMag) and a negative magnet (nMag), both of which exist as monomers in the dark but heterodimerize with each other under blue light (*39*). In OptoTrap, CRY2olig is fused with three copies of pMag, while nMag is fused with a prey protein. Under blue light, CRY2olig-pMag(3x) clusters via the CRY2olig moiety, and nMag-prey is recruited to the cluster via pMag-nMag interaction. By tagging a POI with a bait protein that constitutively binds to the prey, the POI can be recruited into the aggregates (Fig. 1A). In addition to one copy of nMag (1n) fused to the prey, we further developed a variant by fusing the prey to a tandem dimer of nMag (2n). The latter variant is expected to produce larger aggregates due to cross-linking among CRY2olig clusters by pMag-nMag interactions (Fig. 1B) and thus is expected to increase the efficiency of clustering.

To increase the versatility of OptoTrap, we used two prey-bait pairs: NB-GFP (Fig. 1B) and $GFP_{1–10}$-GFP_{11} (Fig. 1C). NB is a high-affinity nanobody against GFP (*40*), while $GFP_{1–10}$ and GFP_{11} are two GFP fragments that automatically reconstitute into a complete fluorescent molecule (*41*). By tagging the POI with several tandem copies of GFP_{11}, POI is predicted to be recruited into aggregates more efficiently and the aggregates are expected to be bigger due to the cross-linking effect (Fig. 1C). In addition, we incorporated two variants of pMag that exhibit different disassociation kinetics: pMag (S) and pMagFast2 (F). The dissociation between pMag and nMag typically takes hours, while pMagFast2 disassociates from nMag within minutes (*39*).

Last, we reasoned that expressing CRY2olig-pMag(3x) at a higher level than that of nMag-prey can potentially result in a more complete recruitment of nMag-prey to CRY2olig-pMag(3x) clusters. Thus, we constructed nMag-prey in a standard upstream activating sequences (UAS) vector (pACU) (*42*) while generating CRY2olig-pMag(3x) in a high-expression UAS vector (pIHEU) (*42*). In total, we generated six OptoTrap variants that differ in the pMag-nMag pair, nMag number, and the prey-bait pair (Table 1). These transgenes can be expressed in a tissue-specific manner in *Drosophila* by Gal4 drivers (*43*).

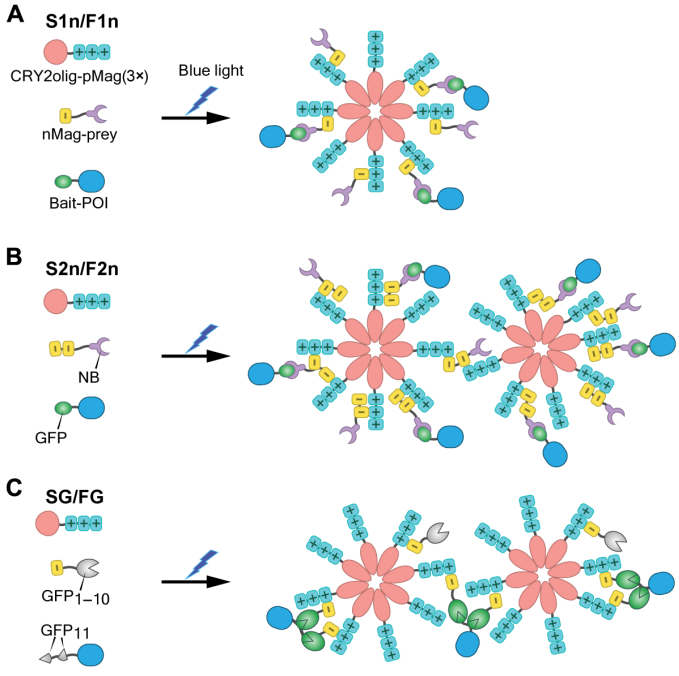

Fig. 1. Design of the OptoTrap system. (**A**) The general design of OptoTrap, exemplified by one-nMag (1n) versions. F1n, CRY2olig-pMagFast2(3x) + mIFP-nMagHigh1-NB; S1n, CRY2olig-pMag(3x) + mIFP-nMagHigh1-NB. (**B**) OptoTrap with two copies of nMag (2n), nanobody (NB) as the prey, and GFP as the bait. S2n, CRY2olig-pMag(3x) + mIFP-nMagHigh1(2X)-NB; F2n, CRY2olig-pMagFast2(3x) + mIFP-nMagHigh1(2X)-NB. (**C**) OptoTrap with $GFP_{1–10}$ as the prey and GFP_{11} as the bait. SG, CRY2olig-pMag(3x) + mIFP-nMagHigh1-$GFP_{1–10}$; FG, CRY2olig-pMagFast2(3x) + mIFP-nMagHigh1-$GFP_{1–10}$. In all variants, mIFP (not shown in the diagram) is fused to the N terminus of nMag-prey for monitoring cluster formation. mIFP, monomeric infrared fluorescent protein.

OptoTrap exhibits light-dependent and reversible aggregation in epithelial cells and neurons

We first assessed the effectiveness of CRY2olig forming light-dependent aggregates in epidermal cells and C4da neurons of *Drosophila* larvae. When using an intermediate epidermal driver (*R15A11-Gal4*), CRY2olig fused to a monomeric infrared fluorescent protein (mIFP) appeared diffused in the cell when kept in the dark but formed clusters upon acute blue laser illumination (Fig. 2A; see Supplementary Text). These clusters mostly dissolved after a 3-hour recovery in the dark (fig. S1A) and returned completely to diffused patterns within 7 hours (fig. S1B). Clusters in these cells could be re-induced by blue laser illumination again (fig. S1, A and B), confirming the reversible nature of CRY2olig aggregation. CRY2olig-mIFP exhibited similar light-dependent clustering in dendritic branches of C4da neurons (Fig. 2B). The half-times ($t_{1/2}$) of aggregation are 8 s in epidermal cells and 4 s in C4da neurons, as measured by the coefficient of variation (Fig. 2C). Unexpectedly, CRY2olig-mIFP formed aggregates even in the dark when a strong epidermal driver (*R16D01-Gal4*) was used (fig. S1C),

Table 1. Variants of OptoTrap.

ID	CRY2olig-pMag*	nMag-Prey†
F1n	CRY2olig-pMagFast2(3x)	mIFP-nMagHigh1-NB
S1n	CRY2olig-pMag(3x)	mIFP-nMagHigh1-NB
F2n	CRY2olig-pMagFast2(3x)	mIFP-nMagHigh1(2X)-NB
S2n	CRY2olig-pMag(3x)	mIFP-nMagHigh1(2X)-NB
FG	CRY2olig-pMagFast2(3x)	mIFP-nMagHigh1-$GFP_{1–10}$
SG	CRY2olig-pMag(3x)	mIFP-nMagHigh1-$GFP_{1–10}$

*CRY2olig-pMag variants are constructed in pIHEU, a high-expression UAS vector. †nMag-Prey variants are constructed in pACU, a regular UAS vector.

suggesting that CRY2olig can form light-independent aggregates at high concentrations in epithelial cells. We did not observe light-independent aggregation of CRY2olig-mIFP in neurons.

We next evaluated the complete OptoTrap system by measuring the recruitment of mIFP-tagged nMag into aggregates. 1n variants produced more obvious aggregates than 2n variants in epidermal cells upon acute illumination by blue laser (Fig. 2D and fig. S1D), while 2n variants are much more effective than 1n variants in neuronal branches (Fig. 2F and fig. S1E). Thus, we used 1n only for epidermal cells and 2n only for neurons in subsequent characterization. Testing blue lasers of different intensities and scanning speeds (fig. S1, F to H), we found that aggregates can be efficiently induced in epidermal cells by 0.02 to 0.2% 488-nm laser (9.8 mW at the full power) scanning at both 600 and 1000 Hz (fig. S1, F and G). The laser could not induce aggregation at 2% power or at 8000 Hz (fig. S1H).

To examine the switch-on kinetics, animals that grew in the dark were subjected to blue laser illumination only in a region of interest (ROI) on the larval body wall. Aggregation of OptoTrap was rapidly and locally induced in the ROI of epidermal cells (Fig. 2D and movie S1) and dendritic branches of neurons (Fig. 2F and movie S2). The half-times of aggregation are slightly faster for the fast variants ($t_{1/2} = 0.5$ s for both F1n in epidermal cells and F2n in neurons) than for the slow variants ($t_{1/2} = 1.2$ s for S1n in epidermal cells and $t_{1/2} = 1.6$ s for S2n in neurons) (Fig. 2, E and G). We also investigated the switch-off kinetics by monitoring the recovery of nMag-mIFP from aggregates to diffused signals (Fig. 2H). The fast variants of OptoTrap had much faster recovery compared to the slow variants: In neurons, F2n showed a $t_{1/2off}$ of 1.6 min, while S2n had a $t_{1/2off}$ of 40 min; in epidermal cells, F1n had a $t_{1/2off}$ of 7.4 min, while S1n had a $t_{1/2off}$ of 65 min (Fig. 2, I and J). Thus, the OptoTrap system contains variants appropriate for investigating biological processes at timescales of minutes to hours in both epithelial cells and neurons.

To better understand protein dynamics within aggregates, we used fluorescence recovery after photobleaching to measure the diffusion kinetics of CRY2olig and nMag separately in epidermal cells. When kept at the aggregated state, CRY2olig-mIFP showed almost no recovery of signals after photobleaching (Fig. 2, K and L), while nMag-mIFP recovered quickly in all four variants of OptoTrap ($t_{1/2} = 13$ s for S1n; 10 s for F1n; 17 s for S2n; 13 s for F2n) to about 80% of the original level (Fig. 2, M and N). These data suggest that CRY2olig proteins are immobile within aggregates, while most nMag proteins can be exchanged among aggregates. This dynamic property of nMag is possibly due to the short lifetime of pMag/nMag binding and will likely prevent the recruited proteins from forming irreversible aggregates (*44*).

OptoTrap can cluster endogenous GFP-tagged proteins under light

Taking advantage of the available GFP-tagged endogenous proteins in *Drosophila*, we tested OptoTrap's versatility in clustering proteins of different sizes and subcellular locations (table S1) in epidermal cells. These proteins include cytoskeleton-binding proteins, mRNA binding proteins, enzymes, motor proteins, and cell-cell junction proteins. OptoTrap^{S1n} was chosen to trap GFP by NB and to visualize OptoTrap-expressing cells by mIFP fluorescence. *en-Gal4* (*45*) was used to express OptoTrap in a strip of epidermal cells in each abdominal segment so that anterior nonexpressing cells can serve as an internal control. We used two light exposure periods: short activation [5 min of illumination by mixed red/green/blue light-emitting diode (LED) lights after growth in the dark] (Fig. 3, A to H) and extended activation (120 hours of chronic LED light exposure throughout embryonic and larval development; see Supplementary Text) (Fig. 3, I to P). We used mixed-color lights for photoactivation because animals develop better under mixed lights than under blue light only. In both methods, we detected OptoTrap-induced aggregates of all proteins in the expression region, which colocalized with OptoTrap. Notably, transmembrane junctional proteins armadillo (Arm) (Fig. 3, E and M) (*46*) and neuroglian (Nrg) (Fig. 3, H and P) were also observed in intracellular puncta colocalizing with OptoTrap. These puncta are possibly caused by endocytosis, as Nrg-GFP puncta colocalized with endosomal markers Rbsn5 and Rab7 (fig. S2, A and B). These data suggest that OptoTrap can aggregate and relocate diverse endogenous proteins in a light-dependent manner.

Activities of GFP-tagged proteins can be manipulated by OptoTrap in epithelial cells and neurons

We next asked whether protein clustering or aggregation induced by OptoTrap can be used to manipulate protein activity by light. Nrg is a component of the septate junction complex (*47*) and is required for the integrity of epithelial septate junctions (*48*). Capable of mediating cell-cell adhesion through homophilic interactions (*49*), Nrg has been proposed to activate the downstream assembly of the cytoskeleton through clustering (*50*). However, no approaches were available previously to directly test this model in vivo. We thus examined the impacts of Nrg-GFP clustering by OptoTrap^{S1n} in a strip of epidermal cells in the middle of every segment (Fig. 4A). Since the *Nrg* locus is on the X chromosome, we examined both heterozygous

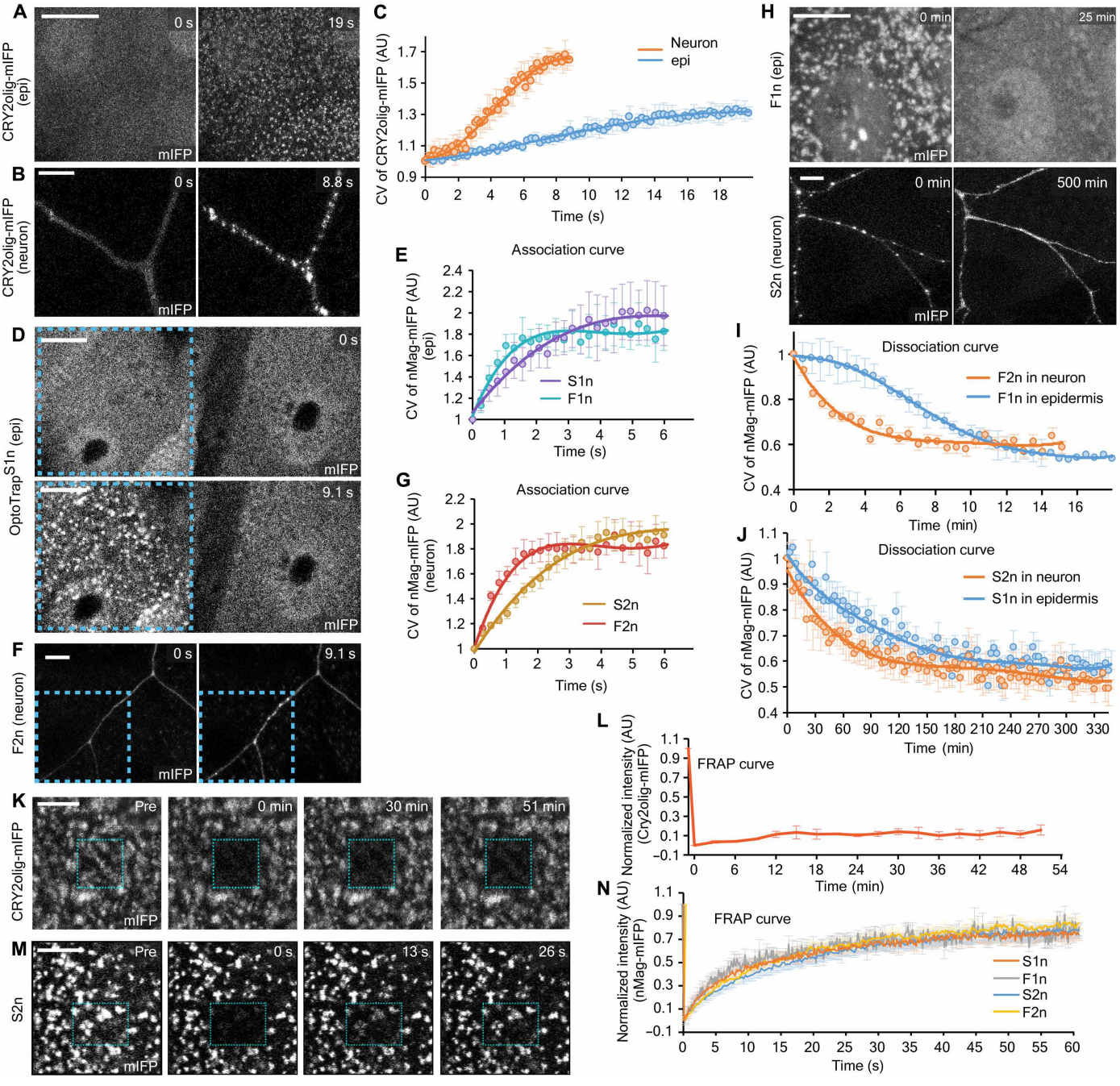

Fig. 2. OptoTrap exhibits light-dependent and reversible aggregation in epithelial cells and neurons. (**A** and **B**) CRY2olig-mIFP in epidermal cells (*Gal4*^{R15A11} > *CRY2olig-mIFP*) (A) and a C4da neuron (*Gal4*^{ppk} > *CRY2olig-mIFP*) (B) before and after blue laser activation. (**C**) Coefficient of variation (CV = SD of mIFP intensity/mean mIFP intensity) of CRY2olig-mIFP in neurons and epidermal cells (epi) plotted over time. $n = 5$ (epi and neuron). (**D**) Epidermal cells in *Gal4*^{R16D01} > *OptoTrap*^{S1n} before and after blue laser activation. The illuminated region is enclosed by the dotted line. OptoTrap is visualized by mIFP. (**E**) CV of OptoTrap mIFP signals in epidermal cells plotted over time. $n = 9$ (S1n) and 7 (F1n). (**F**) A C4da neuron in *Gal4*^{ppk} > *OptoTrap*^{F2n}. The illuminated region is enclosed by the dotted line. (**G**) CV of OptoTrap mIFP signals in C4da neurons plotted over time. $n = 5$ (S2n) and 6 (F2n). (**H**) Dissociation of OptoTrap aggregates in epidermal cells (*Gal4*^{R16D01} > *OptoTrap*^{F1n}) and C4da neurons (*Gal4*^{ppk} > *OptoTrap*^{S2n}). Animals were reared in light but kept in the dark during imaging. (**I** and **J**) CV of mIFP signals in fast (I) and slow (J) versions of OptoTrap in epidermal cells and C4da neurons plotted over time in recovery experiments. $n = 8$ (F1n in epidermis), 5 (F2n in neuron), 4 (S1n in epidermis), and 9 (S2n in neuron). (**K** to **N**) Fluorescence recovery after photobleaching (FRAP) of CRY2olig-mIFP (*Gal4*^{R15A11} > *CRY2olig-mIFP*) [(K) and (L)] and OptoTrap mIFP (*Gal4*^{R16D01} > *OptoTrap*^{S2n}) [(M) and (N)] in epidermal cells. Animals grew in light and were kept in blue light during imaging. Blue rectangles indicate photobleached regions. mIFP intensity was normalized by the first frame. $n = 3$ (CRY2olig-mIFP) and 12 (S1n, F1n, S2n, and F2n). Scale bars, 10 μm. In plots (C), (E), (G), (I), and (J), circles, mean; bars, SD; solid line, fit of the curve. In (B), (F), and (H), *UAS-HO1* was coexpressed in neurons to make mIFP fluorescent. AU, arbitrary units.

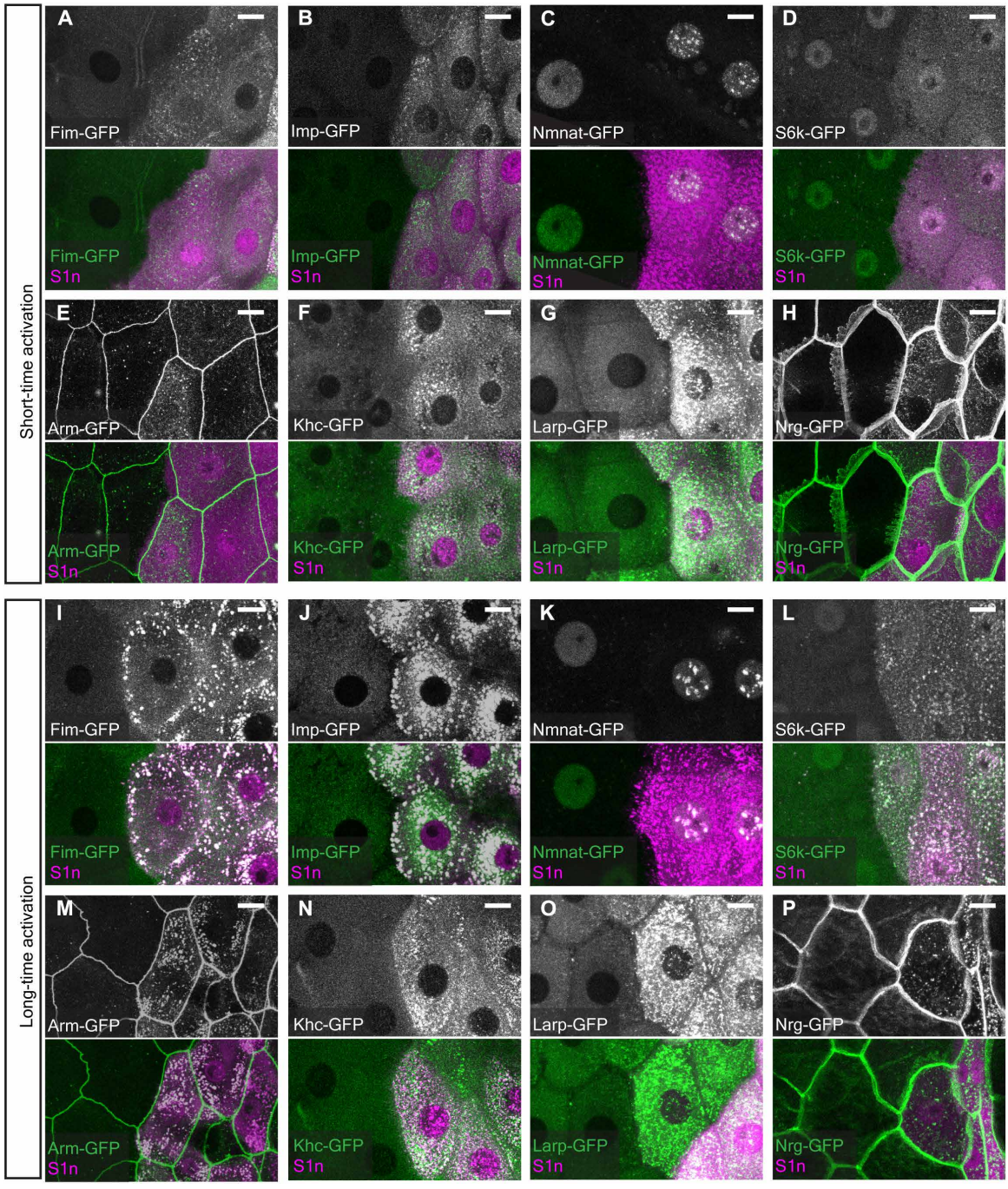

Fig. 3. OptoTrap can cluster endogenous GFP-tagged proteins under blue light. (**A** to **H**) Various GFP-tagged endogenous proteins in *Gal4^{en} > OptoTrap^{S1n}* after 5-min mixed LED light illumination. The OptoTrap-expressing epidermal cells are indicated by mIFP (magenta). Scale bars, 25 μm. (**I** to **P**) GFP-tagged endogenous proteins in *Gal4^{en} > OptoTrap^{S1n}* animals that were reared under mixed LED light since the embryonic stage. Scale bars, 25 μm.

females (*Nrg-GFP/+*), in which half of Nrg proteins are tagged by GFP, and hemizygous males (*Nrg-GFP/Y*), in which all Nrg proteins are tagged. Compared to the control in which only mIFP-nMag-NB was expressed (Fig. 4B), OptoTrap expression in the dark did not affect epidermal cell shape in either *Nrg-GFP* heterozygotes or hemizygotes (Fig. 4, C and H to J). However, after 72 hours of chronic light exposure (through mixed LED light), the OptoTrap-expressing cells were deformed in both heterozygotes and hemizygotes (Fig. 4, D and E). These cells became smaller, as measured by the cell size (Fig. 4H), and narrower, as measured by the circularity and the height/width ratio (Fig. 4, I and J). The hemizygotes appeared to have stronger phenotypes than the heterozygotes, but the differences were not statistically significant. In addition, some epidermal cells became multinucleated (arrows in Fig. 4, E and F), possibly due to cell fusion.

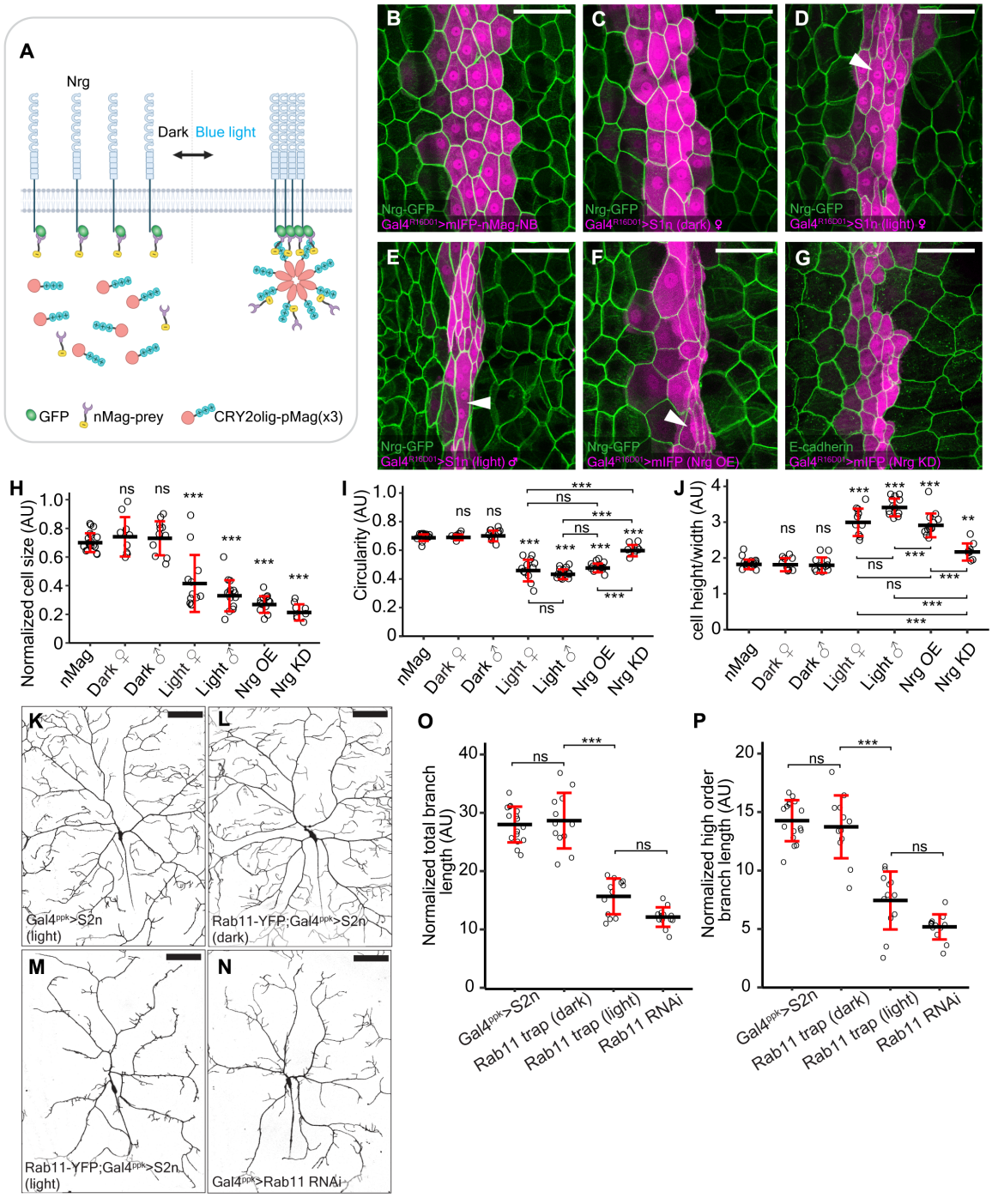

Fig. 4. Activities of GFP-tagged proteins can be manipulated by OptoTrap in epithelial cells and neurons. (**A**) A schematic of Nrg-GFP clustering by OptoTrap. (**B** to **G**) Epidermal cells in *Nrg-GFP; Gal4^{R16D01} > mIFP-nMag-NB* (B), *Nrg-GFP; Gal4^{R16D01} > OptoTrap^{S1n}* grown in the dark (C), *Nrg-GFP; Gal4^{R16D01} > OptoTrap^{S1n}* female grown in light (D), *Nrg-GFP; Gal4^{R16D01} > OptoTrap^{S1n}* male grown in light (E), *Nrg-GFP; Gal4^{R16D01} > UAS-Nrg* (F), and *Gal4^{R16D01} > UAS-Nrg-RNAi* (G). *Gal4^{R16D01}*-expressing cells are indicated by mIFP (magenta). The epidermal cell borders are visualized by Nrg-GFP (B to F) and E-cadherin staining (G). Scale bars, 100 μm. (**H** to **J**) Normalized size [Gal4^{R16D01} cells/wild-type (WT) cells] (H), circularity (I), and height/width ratio (J) of *Gal4^{R16D01}*-expressing epidermal cells. Each circle represents a segment; $n = 18$ for mIFP-nMag-NB (nMag), $n = 9$ for OptoTrap female (dark), $n = 11$ for OptoTrap male (dark), $n = 12$ for OptoTrap female (light), $n = 14$ for OptoTrap male (light), $n = 13$ for Nrg OE, and $n = 8$ for Nrg knockdown (KD). ***$P < 0.001$; **$P < 0.01$; ns, not significant; one-way analysis of variance (ANOVA) and Tukey's honestly significant difference (HSD) test. Black bars, mean; red bars, SD. (**K** to **N**) C4da neurons in *Gal4^{ppk} > OptoTrap^{S2n}* animals reared under light (K), *Rab11-YFP; Gal4^{ppk} > OptoTrap^{S2n}* animals reared in the dark (L) and under light (M), and *Gal4^{ppk} > Rab11 RNAi* animals (N). Neurons were labeled by *Gal4^{ppk} > CD4-tdTom*. Scale bars, 100 μm. (**O** and **P**) Total branch length (O) and high-order branch length (P) (orders 5 to 6) normalized by segment width. Each circle represents a neuron. $n = 16$ for *Gal4^{ppk} > OptoTrap^{S2n}* (light), $n = 12$ for *Rab11-YFP; Gal4^{ppk} > OptoTrap^{S2n}* (both dark and light), and $n = 13$ for *Gal4^{ppk} > Rab11 RNAi*. ***$P < 0.001$; Student's *t* test. Black bars, mean; red bars, SD.

The fact that OptoTrap caused epidermal cell deformation in *Nrg-GFP* heterozygotes suggests that the phenotype is dominant, which is consistent with the hypothesis of clustering-induced Nrg activation. We further examined *Nrg* GOF by OE (*48*) and LOF by knockdown (KD). While Nrg KD caused the strongest reduction of cell size (Fig. 4, G and H), Nrg OE caused multinucleation and cell narrowing more similarly to OptoTrap manipulations (Fig. 4, F and H to J). These data provide supporting, even though not definitive, evidence that clustering induces Nrg activation.

Besides potentially activating proteins by clustering, we reason that OptoTrap may also inhibit a protein by sequestering it and causing its local depletion. To test this possibility, we tried manipulation of Rab11-YFP (*51*) by OptoTrap in C4da neurons because Rab11 is a cytoplasmic guanosine triphosphatase required for dendrite growth of C4da neurons (*52*). We generated *Rab11-YFP* homozygous animals that express OptoTrap^{S2n} in C4da neurons and reared them in constant dark or light conditions. Compared to control neurons that only expressed OptoTrap^{S2n}, these neurons showed 44.0% light-dependent dendrite reduction, including 48.2% reduction of high-order branches (orders 5 to 6), only in the light condition (Fig. 4, K to M, O, and P). These reductions are comparable to the dendritic reductions of *Rab11* KD (Fig. 4, N to P). Thus, our results with Nrg-GFP and Rab11-YFP suggest that OptoTrap can be used to manipulate the activity of endogenous proteins, including membrane proteins, in vivo.

Optogenetic clustering of α-tubulin results in tunable dendrite reduction of neurons

To investigate the role of MTs in dendrite morphogenesis by OptoTrap, we tagged the α-*Tubulin at 84B* (α*Tub84B*) locus with one copy of GFP_{11}. Like GFP-tagged α*Tub84B* (*53*), the α*Tub84B-GFP$_{11}$* allele is male sterile; thus, we were unable to obtain α*Tub84B-GFP$_{11}$* homozygotes. However, we reason that aggregating αTub84B-GFP_{11} that has been incorporated into MTs may still be able to disrupt dynamic MTs, even if not all the α-tubulins are tagged.

To examine αTub84B-GFP_{11} distribution upon OptoTrap activation, we expressed OptoTrap^{SG} in C4da neurons and subjected the larvae to blue light. The expression of nMag-$GFP_{1–10}$ alone resulted in green fluorescence detectable in main dendrite branches (fig. S3A), which contain mainly stable MT bundles (*54*), suggesting successful reconstitution of split GFP. Exposing OptoTrap-expressing larvae to light for 5 min led to stronger GFP signals in these main branches, although the signals still appeared to be continuous (fig. S3B). In contrast, with 72-hour chronic light exposure, GFP signals were predominantly detected in large puncta in main dendrites (fig. S3C), likely due to preferential recruitment of free αTub84B-GFP_{11} into OptoTrap aggregates rather than their assembly into MTs. These data suggest that OptoTrap^{SG} can aggregate αTub84B-GFP_{11}.

To determine how aggregation of α-tubulin affects dendrite morphogenesis, we cultured larvae in the dark for various periods of time, so that GFP_{11}-tagged α-tubulin could be assembled into MTs, and then grew the larvae under light until they were imaged at 120 hours after egg-laying (AEL). As controls, neither expressing OptoTrap^{SG} in wild-type (WT) neurons under light nor expressing nMag-$GFP_{1–10}$ only in α*Tub84B-GFP$_{11}$* heterozygotes caused dendrite reduction (fig. S3, D to H), suggesting that OptoTrap aggregation by itself and the reconstitution of GFP on αTub84B do not affect neuronal morphology. As expected, no dendrite reduction was observed in larvae grown in the dark for the entire time (Fig. 5A and fig. S3, G and H) or for 48 hours before switching to the light (fig. S3, I and J), indicating the absence of light-independent disruption of MTs. However, after larvae were switched from dark to light, we observed various degrees of dendrite reduction (Fig. 5, B to D, G, and H). The most severe reduction was observed in a subset of larvae exposed to light for 72 hours, where high-order dendrites were nearly absent (Fig. 5, D, G, and H). Forty-eight–hour light exposure also induced strong dendrite reduction, mainly due to the shortening and simplification of high-order branches (Fig. 5, C, G, and H). Animals kept in light for 96 hours or longer did not show obvious dendrite reduction (Fig. 5, E to H). A possible explanation for this observation is that, with early activation of OptoTrap, most αTub84B-GFP_{11} proteins are sequestered before they can be assembled into MTs, and thus, high-order branches mostly contain MTs devoid of tagged α-tubulin.

Because MT disruption in the above experiments mainly affected high-order branches, we next used time-lapse imaging (*55*) to examine dendrite dynamics of three types of neurons: WT neurons, neurons with αTub84B-GFP_{11} clustered for 48 hours before imaging under blue laser light (48-hour clustering; see Supplementary Text), and neurons with αTub84B-GFP_{11} being clustered from the beginning of the imaging under blue laser light (acute clustering). Within 4.5 hours, the total dendrite length and the branch number remained unchanged in WT and 48-hour clustering (Fig. 5, I and J, and movies S3 and S4), even though dendrites were reduced in the latter (Fig. 5C). These data suggest that neurons had reached a steady state after 48-hour clustering. In contrast, acute clustering caused immediate retraction of terminal dendrites (movie S5) and this trend continued throughout the imaging period (Fig. 5, I and J), indicating that acute tubulin clustering immediately destabilizes terminal dendrites.

We next wondered whether aggregation of αTub84B-GFP_{11} can disrupt stable and bundled MTs in thick, low-order dendrites, where MTs form tracks for cargo transport (*56*). We thus examined MT-mediated cargo transport in these branches using the CD4-tdTomato (CD4-tdTom) marker (*42*), which should label all membrane vesicles in the secretory pathway. The majority of CD4-tdTom vesicles in WT dendrites were either static or exhibited retrograde motion, and only a small fraction exhibited anterograde or bidirectional (BD) motion (fig. S3, K, L, and N). Acute clustering of αTub84B-GFP_{11} did not change this distribution (fig. S3, K and L). In addition, the distributions of moving vesicle speed were similar in both WT and acutely clustered tubulin dendrites (fig. S3M). Last, we could not detect an obvious difference in the distribution of Futsch (*57*), a maker of stable and bundled MTs, in thick dendrites after 48-hour clustering of αTub84B-GFP_{11} (fig. S3, O and Q). Thus, tubulin clustering does not seem to disrupt stable MTs in thick dendrites, while it can strongly affect dynamic branches.

Optogenetic clustering causes instant, spatially restricted, and reversible inhibition of kinesin motor in dendrites

MT-based transport plays critical roles in dendrite growth and patterning. The (+) end-directed motor kinesin and the (−) end-directed motor dynein work in concert to transport cargo needed for branch growth to proper locations within the dendritic arbor (*1*, *2*). LOF of kinesin and dynein in C4da neurons results in very similar phenotypes of shifting of high-order dendrites toward the cell body (proximal shift) (*56*, *58*), suggesting that certain "branching machinery" relies on the motor system for delivery to the distal dendritic

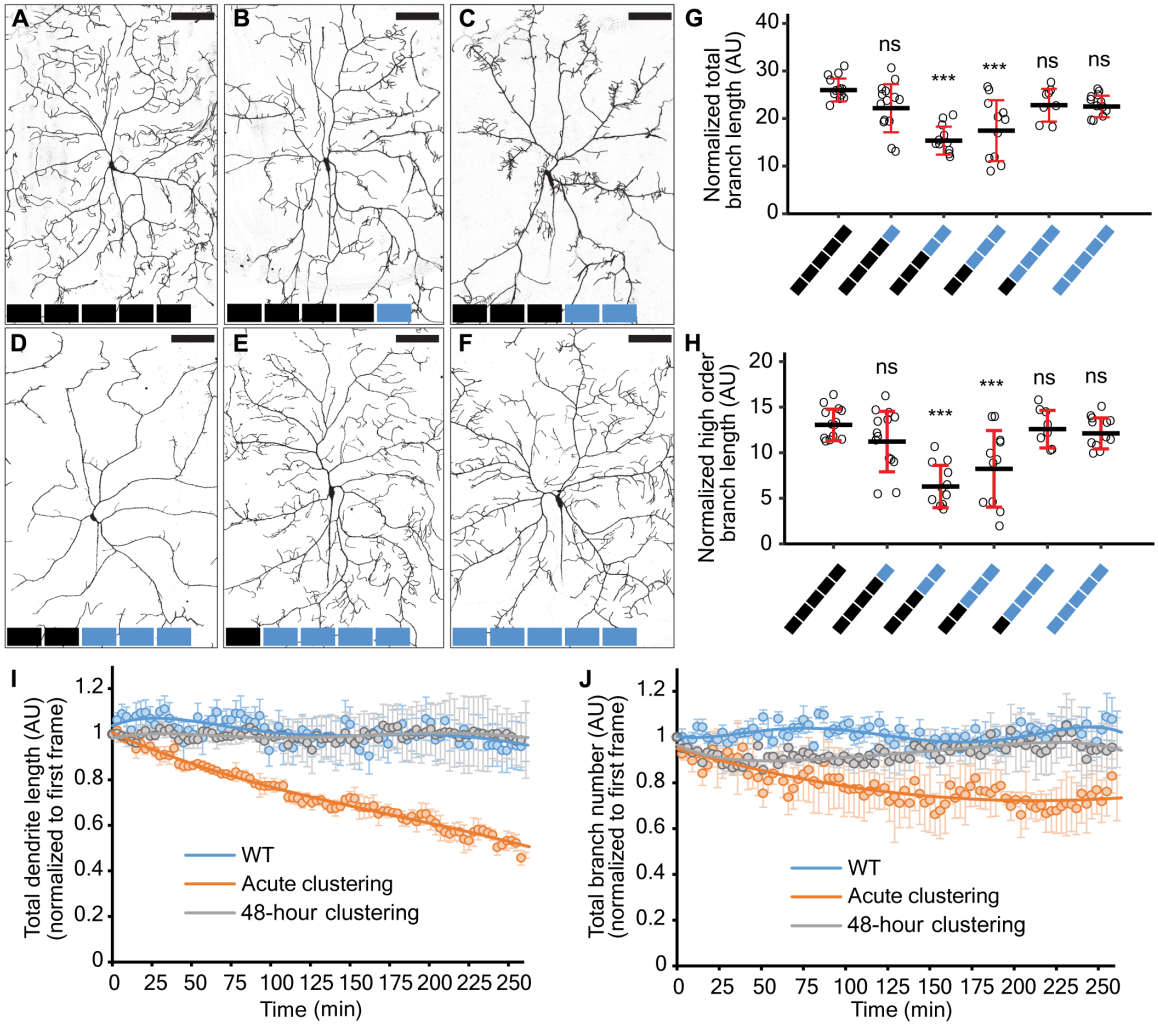

Fig. 5. Optogenetic clustering of α-tubulin results in tunable dendrite reduction of neurons. (**A** to **F**) C4da neurons in *Gal4^{ppk} > OptoTrap^{SG}; α-Tub84B-GFP$_{11}$/+* animals. Neurons were labeled by *Gal4^{ppk} > CD4-tdTom*. Each block represents 24 hours either in dark (black) or light (blue). Scale bars, 100 μm. (**G** and **H**) Total branch length (G) and high-order branch length (H) (orders 5 to 6) normalized by segment width. Each circle represents a neuron; $n = 13$ for 120-hour dark, $n = 14$ for 24-hour light and 96-hour dark, $n = 11$ for 48-hour light and 72-hour dark, $n = 11$ for 72-hour light and 48-hour light, $n = 8$ for 96-hour light and 24-hour dark, and $n = 12$ for 120-hour light. ***$P < 0.001$; one-way ANOVA and Tukey's HSD test. Black bars, mean; red bars, SD. (**I**) Total dendrite length of WT neurons (blue line), neurons with α-Tub84B acute clustering (orange line), and 48-hour clustering (gray line) plotted throughout imaging. The total dendrite length is normalized to that of the first frame. $n = 8$ for WT neuron, $n = 10$ for acute clustering, and $n = 7$ for 48-hour clustering. Circles, mean; bars, SD; solid line, fit of the curve. (**J**) Total branch number of WT neurons (blue line), neurons with α-Tub84B acute clustering (orange line), and 48-hour clustering (gray line) plotted throughout imaging. The total branch number is normalized to that of the first frame. $n = 8$ for WT neuron, $n = 10$ for acute clustering, and $n = 7$ for 48-hour clustering. Circles, mean; bars, SD; solid line, fit of the curve.

arbor. However, how MT-based transport contributes to dendrite growth at different stages of neuronal differentiation remains unknown. To address this question with OptoTrap, we used a *Kinesin heavy chain* (*Khc*) allele tagged with GFP$_{11x7}$ (*59*). Similar to Khc-GFP (Fig. 3F), Khc-GFP$_{11x7}$ can be efficiently clustered in epidermal cells by OptoTrap^{SG} after brief light exposure (fig. S4, A and B). But unlike Khc-GFP, Khc-GFP$_{11x7}$ should allow labeling of kinesin-1 only in neurons. We reasoned that in *Khc-GFP$_{11x7}$* homozygotes, expressing OptoTrap^{FG} in C4da neurons should allow fast clustering and release of all kinesin-1 motors and thus manipulation of kinesin-mediated transport by light.

When visualized by nMag-GFP$_{1–10}$ only, kinesin-1 is broadly distributed throughout the neuron, including distal terminal dendrites (fig. S4, C and I). With OptoTrap^{FG} coexpression, kinesin-1 remained broadly distributed in the arbor when animals grew in the dark (fig. S4, D and I). However, OptoTrap caused Khc to form aggregates in these neurons due to imaging of GFP with the blue laser. These aggregates became brighter and more discrete over a longer period (5 hours) of light exposure, but their locations did not change (fig. S4, E to G), suggesting that kinesin-1 is continuously recruited to and immobilized by OptoTrap aggregates. In comparison, in OptoTrap^{FG}-expressing animals subjected to prolonged light exposure (72 hours), Khc was clustered predominantly in the cell body and sparsely in proximal dendrites, in contrast to its absence in distal dendrites (fig. S4, H and I). These data indicate that OptoTrap efficiently restricts kinesin-1 distribution in neurons in a light-dependent manner.

To test whether Khc clustering is sufficient to inhibit kinesin-1 motor activity, we first examined mitochondrial mobility in dendrites, as mitochondria are cargos of kinesin-1 (*60*). We applied a blue laser to only a portion of the dendrite arbor while imaging mito-mCherry–labeled mitochondria in both illuminated and dark parts of the neuron (Fig. 6A). Mitochondria were found to move in both anterograde and retrograde directions in the dark region (Fig. 6A′) but appeared static in the illuminated part (Fig. 6A″ and movie S6). When the entire animal was illuminated, our quantification shows that the percentage of mitochondria exhibiting directional movement reduced from 33% in the WT to 10% in acute clustering and to 1% in chronic (120 hours) clustering (Fig. 6B). Compared to those in WT neurons, the non-static mitochondria in acute and chronic clustering (nearly all were BD) showed 76 and 85% reduction of speed, respectively (Fig. 6C). Because MTs in da neuron dendrites are primarily in the minus-end-out orientation (*61*), the disruptions to anterograde transport observed above are likely due to indirect trapping of dynein on bidirectionally transported cargos that are also attached to kinesin-1. We next examined the effect of Khc clustering on the transport of CD4-tdTom vesicles. Consistent with kinesin-1 being responsible for retrograde transport, the percentage of retrograde vesicles reduced from 47% in the WT to 9% in acute clustering and 19% in chronic clustering, accompanied by increases of static and BD vesicles from 47% in the WT to 82% in acute clustering and 71% in chronic clustering (Fig. 6, D and E). The average speed of moving CD4-tdTom vesicles was also reduced by 73% in acute clustering and 52% in chronic clustering (Fig. 6, D and F). The above results suggest that kinesin-1 can be inhibited instantaneously, locally, and efficiently by OptoTrap, resulting in disruptions of cargo transport.

Last, we investigated whether the inhibition of kinesin-1 by OptoTrap^{FG} is reversible by examining the recovery of mitochondrial mobility. We first grew larvae under light for 120 hours to keep Khc clustered before imaging mitochondria in the dark. As expected, mitochondria were static at the beginning of switching to the dark, but some mitochondria began to move within 20 min of imaging (Fig. 6G). In a second test, we trapped Khc for 1 hour in late third instar larvae and then recovered the animals in the dark for 5 hours. The mitochondria in recovered neurons showed similar mobilities as those in WT neurons (Fig. 6, B and C). These results suggest that Kinesin-1 can be released from OptoTrap aggregates and become functional again, even after prolonged clustering.

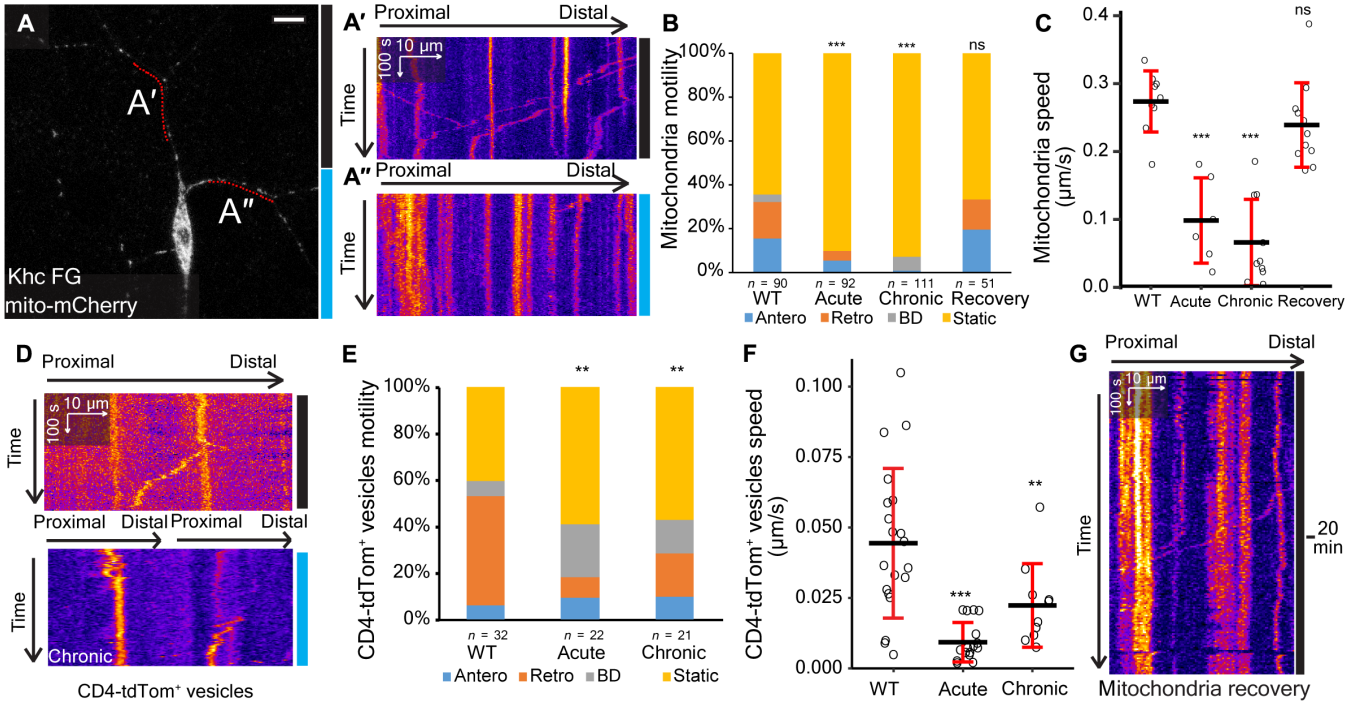

Fig. 6. Optogenetic clustering causes instant, spatially restricted, and reversible inhibition of kinesin motors in dendrites. (**A** and **A**″) A C4da neuron in *Khc-GFP*$_{11x7}$ homozygote that expresses *Gal4*^{ppk} > *OptoTrap*^{FG} and the mitochondrial marker mito-mCherry. The animal was reared in the dark; the bottom half of the neuron was illuminated by a blue laser (blue bar) from the beginning of imaging, and the top half of the neuron remained in the dark (black bar). (**A**′) and (A″) show kymographs of mitochondria in dendrite branches in the dark (A′) and the illuminated region (A″). Scale bars, 10 μm. (**B**) Quantification of mitochondria motility. Sample sizes are indicated in the plot. ***$P < 0.001$; Freeman-Halton extension of Fisher's exact test. (**C**) Speed of mitochondria among the moving (anterograde, retrograde, and bidirectional motion) populations in (B). Each circle represents a neuron. $n = 9$ for WT, $n = 6$ for acute, $n = 12$ for chronic, and $n = 11$ for recovery. ***$P < 0.001$; one-way ANOVA and Tukey's HSD test. Black bars, mean; red bars, SD. (**D**) Kymographs of CD4-tdTom–labeled vesicles in C4da neurons of Khc-GFP$_{11x7}$ homozygote expressing OptoTrap^{FG} that were kept in the dark (top) or reared and imaged in light (bottom). (E) Motility of CD4-tdTom–labeled vesicles. Sample sizes are indicated in the plot. **$P < 0.01$; Freeman-Halton extension of Fisher's exact test. (**F**) Speed of CD4-tdTom–labeled vesicles among the moving (anterograde, retrograde, and bidirectional motion) populations in (E). Each circle represents a vesicle. $n = 20$ for WT, $n = 16$ for instant, and $n = 10$ for chronic. **$P < 0.01$; one-way ANOVA and Tukey's HSD test. Black bars, mean; red bars, SD. (**G**) A kymograph of mitochondria in Khc-GFP$_{11x7}$ homozygote expressing OptoTrap^{FG} that grew in light and kept in the dark while imaging.

Optogenetic clustering reveals temporal and spatial contributions of Khc to dendrite morphogenesis

Having established the effectiveness of OptoTrap in manipulating kinesin-1 activity, we next asked how inhibiting kinesin-1 at different temporal windows may affect the final dendrite pattern. To understand the impacts on the growth of low-order (or primary) versus high-order dendrites and proximal-distal distribution of high-order branches, we measured dendrite arbor size, total branch length, high-order branch length (orders 5 to 6), and radial distribution of high-order branches (from the soma). As negative controls, we first examined OptoTrap^{FG} expression in the WT under light, nMag-GFP$_{1–10}$ expression alone in *Khc-GFP$_{11x7}$* homozygotes, and OptoTrap^{FG} expression in *Khc-GFP$_{11x7}$* homozygotes that were kept in the dark. *Khc-GFP$_{11x7}$* homozygotes in these experiments were derived from *Khc-GFP$_{11x7}$* homozygous mother to eliminate the possible maternal contribution of untagged Khc proteins from the mother's germline, such that all Khc proteins in these animals are tagged (fig. S5I). Like OptoTrap^{SG} (fig. S3, E, G, and H), OptoTrap^{FG} expression in WT neurons did not affect dendrite length or arbor size, except for slightly shifting the radial distribution of high-order branches distally (fig. S5, A and C to F). Expressing nMag-GFP$_{1–10}$ alone in *Khc-GFP$_{11x7}$*, which is expected to make the kinesin-1 motor bulkier, caused a mild dendrite reduction as reflected by the dendrite arbor size (13% reduction) and the total dendrite length (26% reduction) (fig. S5, B to F). Expressing the complete OptoTrap^{FG} in *Khc-GFP$_{11x7}$* homozygotes, when grown in the dark, resulted in a much weaker (17%) dendritic reduction and no changes in arbor size, high-order branch length, or distribution (Fig. 7A and fig. S5, C to F). Thus, we concluded that these minimal impacts on dendrite morphology can serve as a baseline for optogenetic manipulations of Khc. Next, as a positive control where Khc is fully inhibited, we grew animals of the same genotype under light for the entire embryonic and larval period (120 hours). C4da neurons in these animals exhibited a 62% reduction of arbor size, 67% reduction of total branch length, 52% reduction, and strong proximal shift of high-order branches (Fig. 7, F and H to K). These severe defects are consistent with the reported phenotype of *Khc* mutant neurons (*58*), again demonstrating the effectiveness of OptoTrap in inhibiting kinesin-1 in neurons.

Next, to understand the temporal requirements of kinesin-1 in dendrite patterning, we reared animals first in the dark for various durations and then kept them under light until they were imaged at 120 hours AEL (dark-to-light experiments). These light exposure variations did not affect the dendrite morphology of WT neurons (fig. S5, G and H). For neurons in which kinesin-1 was inhibited by OptoTrap, we compared their morphology to those of the baseline (0 hours) and the positive control (120 hours). We observed differential effects on low- and high-order dendrites. First, the increasing length of Khc inhibition was associated with a gradual reduction of the arbor size (Fig. 7, A to H), which is primarily determined by the lengths of low-order branches (1 to 3). This suggests that kinesin-1 supports the growth of low-order branches throughout animal development. Second, unexpectedly, 48, 72, and 96 hours of light exposure resulted in similarly extreme dendrite reduction (69 to 73%) (Fig. 7J), primarily due to similarly severe reductions of high-order branches (70 to 73%) in these groups (Fig. 7I). Third, although all groups exposed to light showed reduction of high-order branches, they exhibited distinct high-order branch distributions: While 24- and 48-hour groups showed uniform reductions throughout the arbor (Fig. 7, B, C, and K), high-order branches in the 96-hour group were clustered near the soma and depleted at the distal arbor (Fig. 7, E and K); the 72-hour group showed an intermediate phenotype (Fig. 7, D and K). These data suggest that early (24 to 48 hours AEL) kinesin-1 activity is necessary for promoting high-order branch growth at the distal arbor, while kinesin-1 activity at later larval development is important for maintaining high-order branches everywhere.

Unexpectedly, we found that 96-hour inhibition caused a stronger reduction and a proximal shift of high-order branches than 120 hours (Fig. 7, E, F, I, and K), even though the latter should induce additional Khc inhibition during the first 24 hours of animal development. To understand the impact of low Khc activity during early neuronal development, we examined *Khc-GFP$_{11x7}$* homozygotes derived from *Khc-GFP$_{11x7}$*/+ heterozygous mothers (HetMo). The neurons in these animals may inherit a small amount of untagged *Khc* mRNA or protein that was deposited maternally into the oocyte (fig. S5I). When grown under light for the whole time, these neurons also showed stronger proximal shift than 120 hours (Fig. 7, F, G, and K), even though both groups showed similar reduction of arbor size and dendrite length (Fig. 7, H to J). These results suggest that maternally contributed Khc can be passed into postmitotic neurons and that residual Khc activity in early neuron development enhances proximal shift and reduction of high-order dendrites.

Next, we asked whether early Khc inhibition has long-lasting effects on the final dendrite pattern or, in other words, whether reactivating Khc later in development can rescue the dendrite defects caused by earlier inactivation. To achieve this, we grew larvae under light for various durations before transferring them to the dark and lastly imaging them at 120 hours AEL (light-to-dark experiments). Like in dark-to-light experiments, we observed differential effects on low- and high-order dendrites. First, inhibiting Khc in the first 3 days produced strong effects on the final arbor size: 24-, 48-, and 72-hour early Khc inhibition resulted in 33, 41, and 61% reduction of the arbor size, respectively (Fig. 7, L to N and P), which are much higher than the 16, 30, and 33% reduction of the arbor size caused by late Khc inhibition for the same lengths (Fig. 7H). Also, further shortening the recovery time below 48 hours did not produce smaller arbors (Fig. 7, O and P). These data suggest that the first 3 days of animal development are the most critical window for arbor growth and that kinesin-1 activity in the last 2 days cannot revert the impacts on the arbor size caused by early inhibition. Second, with increasing lengths of early Khc inhibition (0 to 96 h), we observed increasing degrees of reduction of both total (24 to 56%) and high-order (17 to 58%) branches (Fig. 7, R and Q). However, the dendritic reductions were much weaker than those in dark-to-light experiments with the same durations of Khc inhibition (Fig. 7, J and I). These data suggest that although the growth of high-order branches is cumulative, Khc activity during later neuronal development is more important than early activity in promoting high-order branch growth. With early suppression, relieving kinesin-1 activity for the last 24 hours did not influence the length of total and high-order branches (Fig. 7, O, R, and Q). This suggests that it takes longer than 24 hours for kinesin-1 to recover the support for high-order branch growth. Last, we found that with recovery time longer than 24 hours, high-order branches grew uniformly throughout the arbor (Fig. 7, L to N and S).

Together, the results from our temporal manipulations of Khc suggest that kinesin-1 activity contributes to the growth of low- and

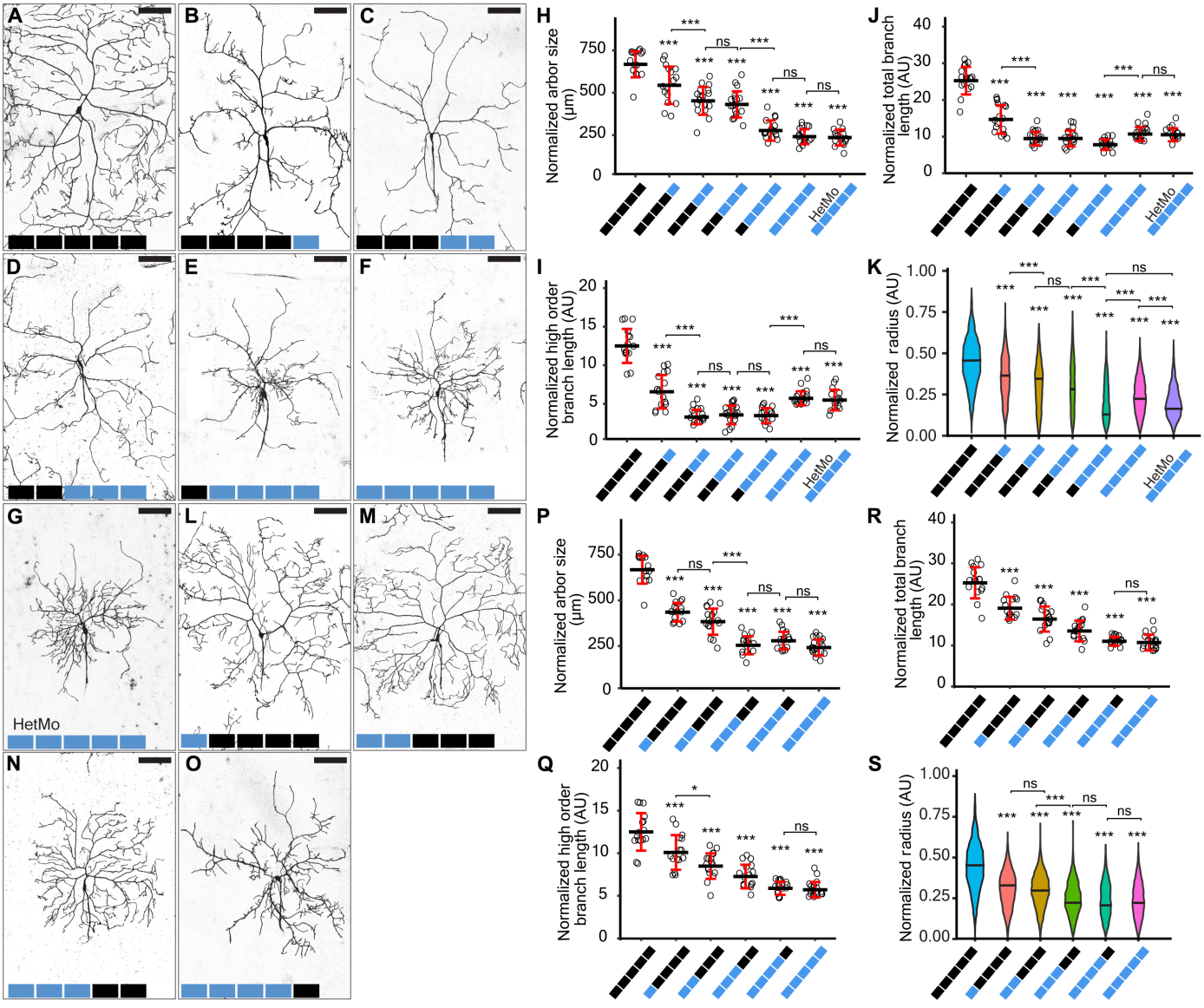

Fig. 7. Optogenetic clustering reveals spatiotemporal contributions of Khc to dendrite morphogenesis. (**A** to **G**) C4da neurons in *Khc-GFP*$_{11x7}$*; Gal4*^{RluA1} > *OptoTrap*^{FG} animals. (**H** to **J**) Arbor size (H), high-order branch length (I), and total branch length (J) of C4da neurons normalized by segment width. Each circle represents a neuron. (**K**) Sholl analysis of high-order branches of C4da neurons. In (H) to (K), $n = 16$ for 120-hour dark, $n = 16$ for 24-hour light and 96-hour dark, $n = 17$ for 48-hour light and 72-hour dark, $n = 18$ for 72-hour light and 48-hour light, $n = 15$ for 96-hour light and 24-hour dark, $n = 18$ for 120-hour light, and $n = 15$ for 120-hour light with heterozygous mother (HetMo). (**L** to **O**) C4da neurons in *Khc-GFP*$_{11x7}$*; Gal4*^{RluA1} > *OptoTrap*^{FG} animals. (**P** to **R**) Arbor size (P), high-order branch length (*70*), and total branch length (R) of C4da neurons normalized by segment width. Each circle represents a neuron. (S) Sholl analysis of high-order branches of C4da neurons. In (P) to (S), $n = 16$ for 120-hour dark, $n = 15$ for 24-hour light and 96-hour dark, $n = 17$ for 48-hour light and 72-hour dark, $n = 16$ for 72-hour light and 48-hour light, $n = 16$ for 96-hour light and 24-hour dark, and $n = 18$ for 120-hour light. The 120-hour dark and 120-hour light datasets are the same as in (H) to (K). In (A) to (G) and (L) to (O), each block represents 24 hours either in dark (black) or light (blue). Neurons were labeled by *ppk-CD4-tdTom*. Scale bars, 100 μm. In (K) and (S), results are presented as violin plots. The radius is measured from the cell body and normalized by segment width. The width of violins correlates with the number of intersections between concentric circles with dendrites at a given radius. For quantifications, $***P < 0.001$; $*P < 0.05$; one-way ANOVA and Tukey's HSD test. Black bars, mean; red bars, SD.

high-order branches differentially in temporal-specific and spatial-specific manners. First, while kinesin-1 promotes the arbor growth during the entire development of the neuron, the first 72 hours are the most critical window that determines the arbor size. Reintroducing Khc activity after this period has little effect on the arbor size. Second, to cause a proximal shift of high-order branches, both persistent suppression of Khc in the last 96 hours and early activity within the first 24 hours of animal development are necessary. Third, kinesin-1 activity in the last 48 hours is necessary for maintaining high-order branches throughout the arbor, but it takes longer than 24 hours for reactivated kinesin-1 to regrow high-order branches.

Optogenetic clustering of Khc disrupts dendrite dynamics

To understand how short-term kinesin-1 inhibition leads to defects of dendrite growth, we examined the dendrite dynamics of C4da neurons in which Khc was acutely inhibited or had been clustered for 24 hours. As expected, WT control neurons did not show net changes in total dendrite length or branch number within 70 min (Fig. 8, A and B, blue line). In contrast, both acute inhibition (Fig. 8, A and B, orange line) and 24-hour inhibition (Fig. 8, A and B, gray line) groups showed gradual and continuous reductions of both total dendrite length and branch number while being imaged under light, with the latter showing higher rates of reduction. These results are consistent with the graded reduction of dendrites caused by increasing durations of Khc inhibition in the dark-to-light experiments (Fig. 7, B to D) and indicate that the retraction of still-dynamic branches speeds up with longer kinesin-1 inhibition, possibly due to increasing local depletion of growth-promoting factors.

Next, to understand how prolonged Khc inhibition affects the kinetics of dendrite dynamics, we examined animals that developed entirely under light, in which high-order branches clustered near the neuronal soma. To visualize the dynamics of dendrites, we mapped the positions of all dendrite tips in each frame (with an interval of 3 min) and projected all time points into a single image. Tip positions were color-coded so that growing and shrinking tips could be distinguished. During a 5-hour period, terminal branches of WT neurons are highly dynamic throughout the arbor (Fig. 8C and movie S7), exhibiting branch elimination (closed arrowheads, indicated by the absence of warm colors), branch addition (open arrowheads, indicated by the absence of cold colors), and repeated retraction and extension (open arrows, indicated by overlapping tracks of cold and warm colors). In contrast, the dendrites of Khc-clustered neurons were much more static (Fig. 8D and movie S8), with more tips exhibiting slow retraction (closed arrows, indicated by distal cold and proximal warm colors). These differences were reflected by measurements of terminal dendrites that persisted within a 150-min window (Fig. 8E). Overall, WT branches showed greater total tip travel distances and had wider net changes of branch length compared to those of Khc-clustered neurons. Together, the above data suggest that kinesin-1 activity is required to support the dynamic growth of dendrites.

Kinesin-1 is required for ER delivery to high-order branches

Rab5-mediated endosomes and Golgi outposts have been previously proposed to be the cargos of kinesin and dynein in supporting dendrite growth. Given that kinesin-1 transports a wide range of cargo, we wondered if other organelles could also be responsible for the dendrite defects caused by *Khc* LOF. We examined endoplasmic reticulum (ER) distribution in dendrites using the ER marker Sec61β-mCherry (*62*) because ER is a cargo of MT motors (*63*). In WT neurons, ER was continuously distributed in both low- and high-order branches, even in proximal segments of terminal dendrites (Fig. 8, F and F′, closed arrowheads). In contrast, in Khc-clustered neurons (Fig. 8, G and G′), ER was almost entirely absent from high-order branches (open arrowheads) and exhibited gaps in low-order branches (arrows). As a result, ER occupied a much smaller portion of dendrites in these neurons as compared to the WT (Fig. 8H). These results suggest that kinesin-1 trapping disrupts the delivery of ER to high-order, including terminal, dendrite branches. Considering that ER plays fundamental roles in many cellular processes, defects in ER delivery could be an important contributing factor to the dendrite phenotypes caused by *Khc* LOF.

DISCUSSION

OptoTrap enables light control of endogenous proteins in *Drosophila*

In this study, we report a protein clustering system that is tailored for in vivo manipulation of endogenous proteins in *Drosophila* by light. This system was designed to offer great versatility and superior spatiotemporal resolution. We demonstrate the effectiveness of this system by clustering and manipulating a range of endogenous proteins in epithelial cells and neurons using transient and spatially restricted light control on isolated animals, as well as prolonged and broad illumination of the whole animal culture during development.

The versatility of this system is expanded by choices at three levels: the prey-bait pair, pMag variants, and the copy number of nMag. First, we engineered two prey-bait pairs: NB/GFP and split GFP fragments. Because many endogenous proteins in *Drosophila* have already been tagged by GFP (*46*, *64*, *65*), the NB versions of OptoTrap can work with these existing, off-the-shelf reagents. On the other hand, the split GFP system offers several unique advantages: (i) Because GFP_{11} is very small (16 amino acids), tagging a protein with even several copies of GFP_{11} usually causes less disruption to protein function than tagging with the full GFP. Thus, GFP_{11}-tagged strains are usually healthier, which can be important for generating homozygotes (in which all proteins of interest are tagged and thus can be clustered) containing OptoTrap and other necessary components. (ii) With GFP_{11} as the tag, the POI can be selectively labeled in specific tissues by expressing $GFP_{1–10}$ only in those tissues (*66*). (iii) Tagging the POI with multiple copies of GFP_{11} can increase the clustering efficiency due to cross-linking among CRY2olig clusters.

Second, we incorporate two variants of pMag that show different association and dissociation kinetics. In practice, these variants show distinct recovery times and allow for manipulation at different temporal scales. The fast variant provides precise temporal and spatial control and thus is suitable for manipulating signaling events with high temporal precision. In contrast, the slow variant is continuously active for hours with a single irradiation, making it ideal for long-term clustering of the POI.

Last, we designed 1X- and 2X-nMag versions for use in different tissues. Our results show that the two versions behave differently in neurons and epidermal cells, likely due to the distinct geometries of the two cell types. Epidermal cells represent cells with simple shapes, whereas neurons have long and slender branches. While 1X-nMag is effective in epidermal cells, 2X-nMag is needed in the limited volume of neuronal branches, likely due to enhanced aggregation by cross-linking.

With OptoTrap, we demonstrated rapid protein clustering at subcellular resolution, such as in part of an epithelial cell and selected branches of a neuron. Designed to manipulate endogenous proteins in model organisms, this system is distinct from most existing optogenetic tools in two ways. First, most previous tools rely on the OE of exogenous designer proteins that produce specific signaling outputs (*14*, *25*, *30*, *44*, *67*). Although these tools are useful for inducing artificial dominant active effects, they are not suitable for revealing the physiological functions of endogenous proteins. In contrast, OptoTrap acts directly on endogenous proteins and can reveal their spatiotemporal requirements in specific cell types.

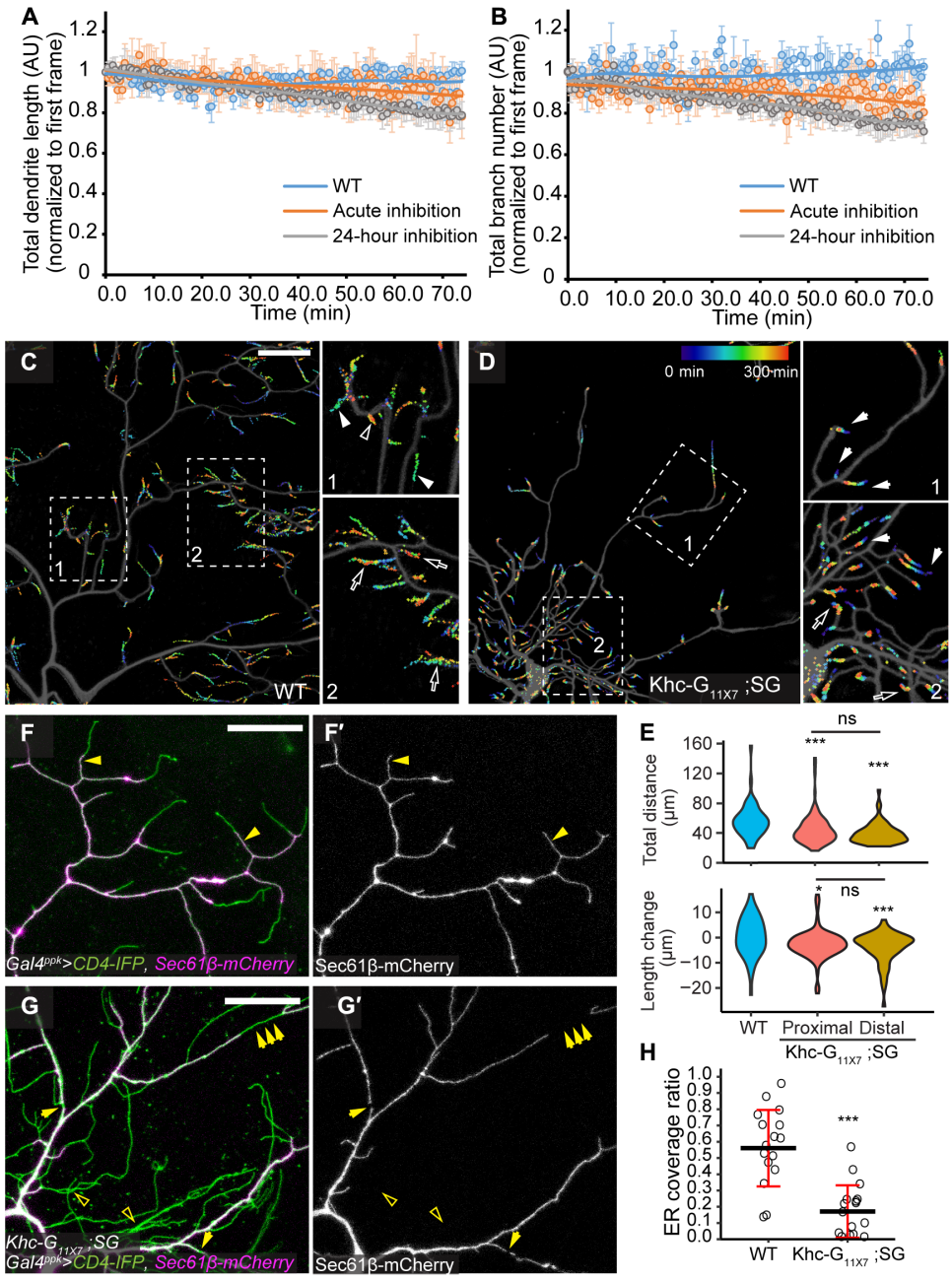

Fig. 8. Optogenetic clustering of Khc disrupts dendrite dynamics and ER delivery to terminal dendrites. (**A** and **B**) Total dendrite length (A) and total branch number (B) of WT neurons (blue), Khc acute inhibited neurons (orange), and Khc 24-hour inhibited neurons (gray) plotted over time. The data were normalized to those of the first frame. $n = 10$ (WT), 9 (acute inhibition), and 9 (24-hour inhibition). Bars, SD. (**C** and **D**) Temporal projections of C4da neurons in WT (C) and *Khc-GFP*$_{11x7}$*; Gal4*^{ppk} > *OptoTrap*^{SG} HetMo reared in constant light (D). Dendrite endings in each frame were marked by a color that corresponds to the temporal sequence of the frame (early, blue; late, red). Open arrowheads indicate newly added branches; closed arrowheads indicate eliminated branches; open arrows indicate branches that exhibited repeated retraction and extension; closed arrows indicate branches that slowly retracted. Scale bars, 25 μm. (**E**) Quantification of cumulative dendrite-tip travel distance (top) and net change of branch length (bottom) over a 150-min window. Branches of *Khc-GFP*$_{11x7}$*; Gal4*^{ppk} > *OptoTrap*^{SG} HetMo neurons were divided into proximal (<95 μm from the soma) and distal (>95 μm from the soma) groups. $n = 49$ (WT), 106 (Khc trap proximal), and 61 (Khc trap distal). (**F** and **G′**) ER distribution in WT [(F) and **F′**] and *Khc-GFP*$_{11x7}$*; Gal4*^{ppk} > *OptoTrap*^{SG} HetMo that were reared in light [**G** and (G′)]. ER was marked Sec61β-mCherry and dendrites were labeled by CD4-IFP. Closed yellow arrowheads indicate ER in terminal branches; open yellow arrowheads indicate the lack of ER in high-order branches; yellow arrows indicate ER breakage in Khc trap neurons. Scale bars, 25 μm. (**H**) ER coverage in high-order branches in WT and Khc trap neurons. Each circle represents a neuron; $n = 16$ (WT) and 16 (Khc trap). For quantifications, ***$P < 0.001$; *$P < 0.05$; one-way ANOVA and Tukey's HSD test.

Second, previous approaches to developing light-controllable agents typically require protein-specific, labor-intensive optimization and hence are difficult to apply to broader proteins. In comparison, the six variants of OptoTrap are sufficient to manipulate a wide range of GFP- or GFP_{11}-tagged proteins. Thus, OptoTrap offers a unique, powerful, and low-cost option for finely dissecting the physiological functions of numerous genes.

Design features and practical factors are important for the application of OptoTrap

Compared to cultured cells, living organisms pose additional challenges for applying optogenetic approaches. Unlike in cultured cells, transgene expression in animals is relatively inflexible and can vary from one cell type to another. An optogenetic system thus needs to be compatible with a wide range of expression levels to be useful for diverse cell types and expression drivers. Like many other light-sensitive modules that show certain degrees of dark activity (*68*), we found that CRY2olig can form light-independent clusters at high expression levels in epithelial cells. The introduction of magnets in the two-step recruitment design of OptoTrap is thus critical for minimizing the system's dark activity: Even if CRY2olig forms clusters in the dark, recruitment of nMag-prey to the clusters still depends on light, ensuring precise control of the POI.

Moreover, we found that the relative expression levels of CRY2olig-pMag(3x) and nMag-prey have a notable impact on the effectiveness of the system. Theoretically, complete recruitment of nMag-prey to CRY2olig-pMag clusters requires overwhelmingly more pMag available for nMag binding. Including three copies of pMag in the CRY2olig-pMag moiety is not sufficient by itself, as our earlier designs of expressing the two parts at similar levels were not effective. Our solution is to express CRY2olig-pMag(3x) with a high-expression UAS vector and nMag-prey with a low-expression UAS vector. Similarly, nMag-prey should be expressed at a much higher level than the POI, which is relatively easy to achieve as the Gal4/UAS-driven nMag-prey is usually expressed more highly than typical endogenous proteins.

When applying OptoTrap, additional considerations are necessary to achieve the desirable outcome. First, OptoTrap operates by clustering the POI, which can affect the activity of different types of proteins differently. For membrane proteins that are activated by oligomerization, OptoTrap may turn on the protein, which possibly applies to Nrg. But for a cytosolic protein whose activity relies on being at a certain subcellular location, such as a motor mediating cargo transport, OptoTrap can inhibit the protein. Thus, OptoTrap can be used to activate or inactivate a protein depending on the mechanism of the protein's function.

Second, at least three control experiments are necessary for an accurate assessment of the results. First, the expression of OptoTrap in WT cells under light is needed to ensure that aggregation of the system is neutral in the cell type of interest. Second, nMag-prey expression in homozygotes of the tagged gene can reveal whether binding of nMag-prey to the POI affects its function. Last, the expression of OptoTrap in homozygotes of the tagged gene in the dark should not produce a strong phenotype and should serve as the baseline for light manipulation.

Last, caution is needed when performing experiments involving regional activation of OptoTrap in intact larvae. While we found that spatially restricted manipulations of OptoTrap are effective in short periods (a few to tens of minutes, depending on the blue laser intensity), the system outside the manipulated regions is sensitive to light scattered by the larval cuticle. In addition, OptoTrap inside the illuminated part of the cell may serve as molecular sinks to continuously recruit OptoTrap and the POI from the dark part of the cell, resulting in local depletion of the POI beyond the illuminated region.

OptoTrap reveals roles of MT in dendrite maintenance

Although MTs are known to be important for neuronal morphogenesis (*1*, *2*), how MTs support the growth of highly dynamic dendritic branches is unclear. Because it is difficult to detect MTs in dynamic terminal dendrite branches, investigating the local role of MTs in dynamic dendrites has been challenging. Traditional LOF approaches lack the spatial and temporal resolution needed to fully address this question. Using OptoTrap, we demonstrate that MTs are required for the maintenance of high-order branches of C4da neurons. In particular, acute clustering of α-tubulin causes immediate retraction of terminal branches. OptoTrap could affect MTs in these branches by sequestering free, tagged tubulin monomers/dimers and/or by directly disrupting dynamic MT filaments that have incorporated tagged α-tubulin. However, we think the reduction of tubulin monomers/dimers (50% at the maximum) alone cannot completely explain the results, as early αTub84B-GFP_{11} clustering (which should reduce α-tubulin concentration and also prevent the incorporation of αTub84B-GFP_{11} into dynamic MT filaments) did not affect high-order branches. Regardless of the exact mechanism, these data are consistent with the idea that MTs do exist in terminal branches and support branch growth by mediating cargo transport and/or by providing mechanical support. The presence of ER in WT terminal dendrites, which is dependent on kinesin-1, further indicates that MT-mediated cargo transport occurs in terminal dendrites. Because markers for stable and bundled MTs cannot be detected in those branches (*54*), MTs are more likely individual and dynamic filaments that are easily disrupted by OptoTrap.

OptoTrap reveals spatiotemporal requirements of kinesin-1 in dendrite patterning

MTs contribute to neuronal morphogenesis by supporting motor-based cargo transport, which is demonstrated by the notable dendrite phenotypes of *khc* and *dynein* mutant neurons (*56*, *58*). Although kinesin-1 and dynein are expected to transport cargos in opposite directions on the polarized MTs in da neuron dendrites (*61*), the LOF of these motors results in highly similar phenotypes because they are interdependent (*58*, *69*). How these motors contribute to dendrite growth at different stages of neuronal differentiation could not be addressed by conventional methods. Using OptoTrap to perturb Khc in different temporal windows of C4da dendrite growth, we found that kinesin-1 affects the final patterns of low- and high-order branches differentially in a temporal-specific manner: For the growth of low-order branches, which correlates with the arbor size, kinesin-1 is more important in the first 72 hours; in contrast, the last 48 hours of neuronal development is the critical window for the growth of high-order branches. In addition, while 48 to 72 hours are minimally required for reactivated kinesin-1 to rescue the growth of low-order branches, 24 to 48 hours of kinesin-1 recovery is sufficient for reactivating the growth of high-order branches. A possible explanation for these differences is that the growth of low- and high-order branches requires different cargos that are transported at unequal rates. Because it takes less than 30 min to relieve kinesin-1 inhibition, and possibly that of dynein, delivery of critical cargos from the cell body

may take >48 hours for low-order branches and >24 hours for high-order branches.

Our time-lapse imaging experiments provided additional clues on how kinesin-1 supports dendrite growth. We found that kinesin-1 is required for the dynamic growth of dendrites. Increasing length of inhibition results in faster retraction of dynamic branches, likely due to more severe local depletion of growth-promoting cargos. Prolonged kinesin-1 inhibition further leads to mostly static or slowly retracting dendrite tips. Mechanistically, in addition to the previously reported cargos Rab5-positive endosomes and Golgi outposts (*56*, *58*, *59*), we found that ER is a cargo that requires kinesin-1 (and likely dynein as well) for delivery to terminal dendrites and for its integrity in low-order branches. Because ER is involved in many fundamental cellular activities, the ER abnormalities caused by kinesin-1 clustering could contribute substantially to dendrite defects.

Furthermore, our experiments reveal a temporal requirement of kinesin-1 in affecting the spatial distribution of high-order branches. Although the proximal shift of high-order branches is a hallmark of kinesin-1 mutant clones (*58*), to produce this phenotype, both persistent suppression in the last 96 hours and early activity in the first 24 hours are necessary. Counterintuitively, additional suppression of kinesin-1 in the first 24 hours (as in the 120-hour light group) results in weaker proximal shift and milder dendrite reduction. A possible explanation is that complete suppression of kinesin-1 in newly born neurons enhances the activities of other kinesins that could partially compensate for the loss of kinesin-1, while kinesin-1 activity in the first 24 hours suppresses such compensatory mechanisms. Following this reasoning, *Khc* mutant C4da clones in otherwise heterozygous animals can generate consistent dendrite proximal shift (*58*) possibly due to residual WT Khc proteins inherited from neuronal progenitor cells at the time of clone generation. Two other observations are also consistent with the possible activities of other kinesins. First, even in complete suppression of kinesin-1, ER can still be delivered into low-order branches. Second, even in the worst phenotype of kinesin-1 LOF, neurons are still able to grow dendritic arbors spanning more than 200 μm. These phenomena can unlikely be explained by diffusion alone.

Last, our comparison of animals derived from homozygous mothers and HetMo showed that postmitotic neurons can inherit maternally contributed kinesin-1 and that this presumably residual amount of kinesin-1 can affect dendrite patterns. Because OptoTrap can access all endogenous proteins in a cell, if they are all tagged as illustrated in this example, to our knowledge, OptoTrap is the only known method that can eliminate the effects of maternal contribution and perdurance at the single-cell level.

OptoTrap can possibly be applied to other systems

In principle, OptoTrap can be applied to other tissues in *Drosophila*, if those tissues can be penetrated by blue light. We found that OptoTrap can even be activated in body wall tissues of freely growing larvae in normal media under ambient light while displaying very little dark activity. The tight control, versatility, and cell type specificity of the system make it a potentially powerful tool for dissecting many developmental processes in vivo. Being modular, the prey-bait pair in the system can be replaced to accommodate endogenous proteins containing other tags. OptoTrap may also be applied to other model organisms that are amenable to transgenic expression and light access.

MATERIALS AND METHODS

The details of fly strains used in this study are listed in the Key Resource Table (table S2). For expression in epidermal cells, we use $Gal4^{R15A11}$ as an intermediate driver and $Gal4^{R16D01}$ and $Gal4^{en}$ as strong drivers that are expressed in strips of epidermal cells. For expression in C4da neurons, we used $Gal4^{ppk}$, except in Fig. 7 and fig. S5 where we used $Gal4^{21-7}$, because $Khc\text{-}GFP_{11x7}$ homozygotes with $Gal4^{ppk}$ were lethal. See Supplementary Text for details of molecular cloning and transgenic flies, live imaging, photoactivation, immunostaining, image analysis and quantification, and statistical analysis.

Supplementary Materials

The PDF file includes:
Supplementary Text
Figs. S1 to S5
Tables S1 and S2
Legends for movies S1 to S8

Other Supplementary Material for this manuscript includes the following:
Movies S1 to S8

REFERENCES AND NOTES

1. M. T. Kelliher, H. A. Saunders, J. Wildonger, Microtubule control of functional architecture in neurons. *Curr. Opin. Neurobiol.* **57**, 39–45 (2019).
2. M. K. Iwanski, L. C. Kapitein, Cellular cartography: Towards an atlas of the neuronal microtubule cytoskeleton. *Front. Cell Dev. Biol.* **11**, 1052245 (2023).
3. C. Conde, A. Caceres, Microtubule assembly, organization and dynamics in axons and dendrites. *Nat. Rev. Neurosci.* **10**, 319–332 (2009).
4. C. Delandre, R. Amikura, A. W. Moore, Microtubule nucleation and organization in dendrites. *Cell Cycle* **15**, 1685–1692 (2016).
5. A. Dema, R. Charafeddine, S. Rahgozar, J. van Haren, T. Wittmann, Growth cone advance requires EB1 as revealed by genomic replacement with a light-sensitive variant. *eLife* **12**, e84143 (2023).
6. G. Y. Liu, S.-C. Chen, G.-H. Lee, K. Shaiv, P.-Y. Chen, H. Cheng, S.-R. Hong, W.-T. Yang, S.-H. Huang, Y.-C. Chang, H.-C. Wang, C.-L. Kao, P.-C. Sun, M.-H. Chao, Y.-Y. Lee, M.-J. Tang, Y.-C. Lin, Precise control of microtubule disassembly in living cells. *EMBO J.* **41**, e110472 (2022).
7. J. C. M. Meiring, I. Grigoriev, W. Nijenhuis, L. C. Kapitein, A. Akhmanova, Opto-katanin, an optogenetic tool for localized, microtubule disassembly. *Curr. Biol.* **32**, 4660–4674.e6 (2022).
8. W. Lu, M. Lakonishok, R. Liu, N. Billington, A. Rich, M. Glotzer, J. R. Sellers, V. I. Gelfand, Competition between kinesin-1 and myosin-V defines *Drosophila* posterior determination. *eLife* **9**, e54216 (2020).
9. W. Nijenhuis, M. M. P. van Grinsven, L. C. Kapitein, An optimized toolbox for the optogenetic control of intracellular transport. *J. Cell Biol.* **219**, e201907149 (2020).
10. Y. I. Wu, X. Wang, L. He, D. Montell, K. M. Hahn, Spatiotemporal control of small GTPases with light using the LOV domain. *Methods Enzymol.* **497**, 393–407 (2011).
11. L. Z. Fan, M. Z. Lin, Optical control of biological processes by light-switchable proteins. *Wiley Interdiscip. Rev. Dev. Biol.* **4**, 545–554 (2015).
12. E. Kwon, W. D. Heo, Optogenetic tools for dissecting complex intracellular signaling pathways. *Biochem. Biophys. Res. Commun.* **527**, 331–336 (2020).
13. K. Zhang, B. Cui, Optogenetic control of intracellular signaling pathways. *Trends Biotechnol.* **33**, 92–100 (2015).
14. Y. I. Wu, D. Frey, O. I. Lungu, A. Jaehrig, I. Schlichting, B. Kuhlman, K. M. Hahn, A genetically encoded photoactivatable Rac controls the motility of living cells. *Nature* **461**, 104–108 (2009).
15. K. M. Bonger, R. Rakhit, A. Y. Payumo, J. K. Chen, T. J. Wandless, General method for regulating protein stability with light. *ACS Chem. Biol.* **9**, 111–115 (2014).
16. F. Paonessa, S. Criscuolo, S. Sacchetti, D. Amoroso, H. Scarongella, F. Pecoraro Bisogni, E. Carminati, G. Pruzzo, L. Maragliano, F. Cesca, F. Benfenati, Regulation of neural gene transcription by optogenetic inhibition of the RE1-silencing transcription factor. *Proc. Natl. Acad. Sci. U.S.A.* **113**, E91–E100 (2016).
17. N. Kim, J. M. Kim, M. Lee, C. Y. Kim, K. Y. Chang, W. D. Heo, Spatiotemporal control of fibroblast growth factor receptor signals by blue light. *Chem. Biol.* **21**, 903–912 (2014).

18. T. Kyung, S. Lee, J. E. Kim, T. Cho, H. Park, Y. M. Jeong, D. Kim, A. Shin, S. Kim, J. Baek, J. Kim, N. Y. Kim, D. Woo, S. Chae, C. H. Kim, H. S. Shin, Y. M. Han, D. Kim, W. D. Heo, Optogenetic control of endogenous Ca^{2+} channels in vivo. *Nat. Biotechnol.* **33**, 1092–1096 (2015).
19. L. J. Bugaj, A. T. Choksi, C. K. Mesuda, R. S. Kane, D. V. Schaffer, Optogenetic protein clustering and signaling activation in mammalian cells. *Nat. Methods* **10**, 249–252 (2013).
20. S. Lee, H. Park, T. Kyung, N. Y. Kim, S. Kim, J. Kim, W. D. Heo, Reversible protein inactivation by optogenetic trapping in cells. *Nat. Methods* **11**, 633–636 (2014).
21. M. K. Nguyen, C. Y. Kim, J. M. Kim, B. O. Park, S. Lee, H. Park, W. D. Heo, Optogenetic oligomerization of Rab GTPases regulates intracellular membrane trafficking. *Nat. Chem. Biol.* **12**, 431–436 (2016).
22. M. J. Kennedy, R. M. Hughes, L. A. Peteya, J. W. Schwartz, M. D. Ehlers, C. L. Tucker, Rapid blue-light-mediated induction of protein interactions in living cells. *Nat. Methods* **7**, 973–975 (2010).
23. D. Yu, H. Lee, J. Hong, H. Jung, Y. Jo, B. H. Oh, B. O. Park, W. D. Heo, Optogenetic activation of intracellular antibodies for direct modulation of endogenous proteins. *Nat. Methods* **16**, 1095–1100 (2019).
24. H. Jung, S. W. Kim, M. Kim, J. Hong, D. Yu, J. H. Kim, Y. Lee, S. Kim, D. Woo, H. S. Shin, B. O. Park, W. D. Heo, Noninvasive optical activation of Flp recombinase for genetic manipulation in deep mouse brain regions. *Nat. Commun.* **10**, 314 (2019).
25. J. E. Toettcher, O. D. Weiner, W. A. Lim, Using optogenetics to interrogate the dynamic control of signal transmission by the Ras/Erk module. *Cell* **155**, 1422–1434 (2013).
26. G. Guntas, R. A. Hallett, S. P. Zimmerman, T. Williams, H. Yumerefendi, J. E. Bear, B. Kuhlman, Engineering an improved light-induced dimer (iLID) for controlling the localization and activity of signaling proteins. *Proc. Natl. Acad. Sci. U.S.A.* **112**, 112–117 (2015).
27. S. Konermann, M. D. Brigham, A. Trevino, P. D. Hsu, M. Heidenreich, L. Cong, R. J. Platt, D. A. Scott, G. M. Church, F. Zhang, Optical control of mammalian endogenous transcription and epigenetic states. *Nature* **500**, 472–476 (2013).
28. X. Wang, L. He, Y. I. Wu, K. M. Hahn, D. J. Montell, Light-mediated activation reveals a key role for Rac in collective guidance of cell movement in vivo. *Nat. Cell Biol.* **12**, 591–597 (2010).
29. S. L. McDaniel, T. J. Gibson, K. N. Schulz, M. Fernandez Garcia, M. Nevil, S. U. Jain, P. W. Lewis, K. S. Zaret, M. M. Harrison, Continued activity of the pioneer factor Zelda is required to drive zygotic genome activation. *Mol. Cell* **74**, 185–195.e4 (2019).
30. H. E. Johnson, J. E. Toettcher, Signaling dynamics control cell fate in the early *Drosophila* embryo. *Dev. Cell* **48**, 361–370.e3 (2019).
31. A. P. Singh, P. Wu, S. Ryabichko, J. Raimundo, M. Swan, E. Wieschaus, T. Gregor, J. E. Toettcher, Optogenetic control of the Bicoid morphogen reveals fast and slow modes of gap gene regulation. *Cell Rep.* **38**, 110543 (2022).
32. V. V. Krishnamurthy, H. Hwang, J. Fu, J. Yang, K. Zhang, Optogenetic control of the canonical Wnt signaling pathway during *Xenopus laevis* embryonic development. *J. Mol. Biol.* **433**, 167050 (2021).
33. J. M. Harris, A. Y. Wang, J. Boulanger-Weill, C. Santoriello, S. Foianini, J. W. Lichtman, L. I. Zon, P. Arlotta, Long-range optogenetic control of axon guidance overcomes developmental boundaries and defects. *Dev. Cell* **53**, 577–588.e7 (2020).
34. Q. Wang, H. Fan, F. Li, S. S. Skeeters, V. V. Krishnamurthy, Y. Song, K. Zhang, Optical control of ERK and AKT signaling promotes axon regeneration and functional recovery of PNS and CNS in *Drosophila*. *eLife* **9**, e57395 (2020).
35. X. Qin, B. O. Park, J. Liu, B. Chen, V. Choesmel-Cadamuro, K. Belguise, W. D. Heo, X. Wang, Cell-matrix adhesion and cell-cell adhesion differentially control basal myosin oscillation and Drosophila egg chamber elongation. *Nat. Commun.* **8**, 14708 (2017).
36. W. B. Grueber, B. Ye, A. W. Moore, L. Y. Jan, Y. N. Jan, Dendrites of distinct classes of *Drosophila* sensory neurons show different capacities for homotypic repulsion. *Curr. Biol.* **13**, 618–626 (2003).
37. A. Taslimi, J. D. Vrana, D. Chen, S. Borinskaya, B. J. Mayer, M. J. Kennedy, C. L. Tucker, An optimized optogenetic clustering tool for probing protein interaction and function. *Nat. Commun.* **5**, 4925 (2014).
38. P. Mas, P. F. Devlin, S. Panda, S. A. Kay, Functional interaction of phytochrome B and cryptochrome 2. *Nature* **408**, 207–211 (2000).
39. F. Kawano, H. Suzuki, A. Furuya, M. Sato, Engineered pairs of distinct photoswitches for optogenetic control of cellular proteins. *Nat. Commun.* **6**, 6256 (2015).
40. A. Kirchhofer, J. Helma, K. Schmidthals, C. Frauer, S. Cui, A. Karcher, M. Pellis, S. Muyldermans, C. S. Casas-Delucchi, M. C. Cardoso, H. Leonhardt, K. P. Hopfner, U. Rothbauer, Modulation of protein properties in living cells using nanobodies. *Nat. Struct. Mol. Biol.* **17**, 133–138 (2010).
41. S. Cabantous, T. C. Terwilliger, G. S. Waldo, Protein tagging and detection with engineered self-assembling fragments of green fluorescent protein. *Nat. Biotechnol.* **23**, 102–107 (2005).
42. C. Han, L. Y. Jan, Y. N. Jan, Enhancer-driven membrane markers for analysis of nonautonomous mechanisms reveal neuron-glia interactions in *Drosophila*. *Proc. Natl. Acad. Sci. U.S.A.* **108**, 9673–9678 (2011).
43. A. H. Brand, N. Perrimon, Targeted gene expression as a means of altering cell fates and generating dominant phenotypes. *Development* **118**, 401–415 (1993).
44. E. M. Zhao, N. Suek, M. Z. Wilson, E. Dine, N. L. Pannucci, Z. Gitai, J. L. Avalos, J. E. Toettcher, Light-based control of metabolic flux through assembly of synthetic organelles. *Nat. Chem. Biol.* **15**, 589–597 (2019).
45. C. Han, D. Yan, T. Y. Belenkaya, X. Lin, *Drosophila* glypicans Dally and Dally-like shape the extracellular Wingless morphogen gradient in the wing disc. *Development* **132**, 667–679 (2005).
46. N. Lowe, J. S. Rees, J. Roote, E. Ryder, I. M. Armean, G. Johnson, E. Drummond, H. Spriggs, J. Drummond, J. P. Magbanua, H. Naylor, B. Sanson, R. Bastock, S. Huelsmann, V. Trovisco, M. Landgraf, S. Knowles-Barley, J. D. Armstrong, H. White-Cooper, C. Hansen, R. G. Phillips, UK Drosophila Protein Trap Screening Consortium, K. S. Lilley, S. Russell, D. S. Johnston, Analysis of the expression patterns, subcellular localisations and interaction partners of *Drosophila* proteins using a *pigP* protein trap library. *Development* **141**, 3994–4005 (2014).
47. J. L. Genova, R. G. Fehon, Neuroglian, Gliotactin, and the Na^+/K^+ ATPase are essential for septate junction function in *Drosophila*. *J. Cell Biol.* **161**, 979–989 (2003).
48. J. Wei, M. Hortsch, S. Goode, Neuroglian stabilizes epithelial structure during *Drosophila* oogenesis. *Dev. Dyn.* **230**, 800–808 (2004).
49. M. Hortsch, Y. M. Wang, Y. Marikar, A. J. Bieber, The cytoplasmic domain of the *Drosophila* cell adhesion molecule neuroglian is not essential for its homophilic adhesive properties in S2 cells. *J. Biol. Chem.* **270**, 18809–18817 (1995).
50. G. Jefford, R. R. Dubreuil, Receptor clustering drives polarized assembly of ankyrin. *J. Biol. Chem.* **275**, 27726–27732 (2000).
51. S. Dunst, T. Kazimiers, F. von Zadow, H. Jambor, A. Sagner, B. Brankatschk, A. Mahmoud, S. Spannl, P. Tomancak, S. Eaton, M. Brankatschk, Endogenously tagged rab proteins: A resource to study membrane trafficking in *Drosophila*. *Dev. Cell* **33**, 351–365 (2015).
52. R. Kramer, S. Rode, S. Rumpf, Rab11 is required for neurite pruning and developmental membrane protein degradation in *Drosophila* sensory neurons. *Dev. Biol.* **451**, 68–78 (2019).
53. B. V. Jenkins, H. A. J. Saunders, H. L. Record, D. M. Johnson-Schlitz, J. Wildonger, Effects of mutating α-tubulin lysine 40 on sensory dendrite development. *J. Cell Sci.* **130**, 4120–4131 (2017).
54. A. R. Poe, L. Tang, B. Wang, Y. Li, M. L. Sapar, C. Han, Dendritic space-filling requires a neuronal type-specific extracellular permissive signal in *Drosophila*. *Proc. Natl. Acad. Sci. U.S.A.* **114**, E8062–E8071 (2017).
55. H. Ji, C. Han, LarvaSPA, a method for mounting *Drosophila* larva for long-term time-lapse imaging. *J. Vis. Exp.* e60792 (2020).
56. Y. Zheng, J. Wildonger, B. Ye, Y. Zhang, A. Kita, S. H. Younger, S. Zimmerman, L. Y. Jan, Y. N. Jan, Dynein is required for polarized dendritic transport and uniform microtubule orientation in axons. *Nat. Cell Biol.* **10**, 1172–1180 (2008).
57. T. Hummel, K. Krukkert, J. Roos, G. Davis, C. Klambt, Drosophila Futsch/22C10 is a MAP1B-like protein required for dendritic and axonal development. *Neuron* **26**, 357–370 (2000).
58. D. Satoh, D. Sato, T. Tsuyama, M. Saito, H. Ohkura, M. M. Rolls, F. Ishikawa, T. Uemura, Spatial control of branching within dendritic arbors by dynein-dependent transport of Rab5-endosomes. *Nat. Cell Biol.* **10**, 1164–1171 (2008).
59. M. T. Kelliher, Y. Yue, A. Ng, D. Kamiyama, B. Huang, K. J. Verhey, J. Wildonger, Autoinhibition of kinesin-1 is essential to the dendrite-specific localization of Golgi outposts. *J. Cell Biol.* **217**, 2531–2547 (2018).
60. A. D. Pilling, D. Horiuchi, C. M. Lively, W. M. Saxton, Kinesin-1 and Dynein are the primary motors for fast transport of mitochondria in *Drosophila* motor axons. *Mol. Biol. Cell* **17**, 2057–2068 (2006).
61. M. C. Stone, F. Roegiers, M. M. Rolls, Microtubules have opposite orientation in axons and dendrites of *Drosophila* neurons. *Mol. Biol. Cell* **19**, 4122–4129 (2008).
62. N. Ferrandiz, L. Downie, G. P. Starling, S. J. Royle, Endomembranes promote chromosome missegregation by ensheathing misaligned chromosomes. *J. Cell Biol.* **221**, e202203021 (2022).
63. J. Lippincott-Schwartz, T. H. Roberts, K. Hirschberg, Secretory protein trafficking and organelle dynamics in living cells. *Annu. Rev. Cell Dev. Biol.* **16**, 557–589 (2000).
64. D. Li-Kroeger, O. Kanca, P. T. Lee, S. Cowan, M. T. Lee, M. Jaiswal, J. L. Salazar, Y. He, Z. Zuo, H. J. Bellen, An expanded toolkit for gene tagging based on MiMIC and scarless CRISPR tagging in *Drosophila*. *eLife* **7**, e38709 (2018).
65. K. J. Venken, K. L. Schulze, N. A. Haelterman, H. Pan, Y. He, M. Evans-Holm, J. W. Carlson, R. W. Levis, A. C. Spradling, R. A. Hoskins, H. J. Bellen, MiMIC: A highly versatile transposon insertion resource for engineering *Drosophila melanogaster* genes. *Nat. Methods* **8**, 737–743 (2011).
66. D. Kamiyama, S. Sekine, B. Barsi-Rhyne, J. Hu, B. Chen, L. A. Gilbert, H. Ishikawa, M. D. Leonetti, W. F. Marshall, J. S. Weissman, B. Huang, Versatile protein tagging in cells with split fluorescent protein. *Nat. Commun.* **7**, 11046 (2016).

67. J. Shao, M. Wang, G. Yu, S. Zhu, Y. Yu, B. C. Heng, J. Wu, H. Ye, Synthetic far-red light-mediated CRISPR-dCas9 device for inducing functional neuronal differentiation. *Proc. Natl. Acad. Sci. U.S.A.* **115**, E6722–E6730 (2018).
68. G. Miesenbock, Optogenetic control of cells and circuits. *Annu. Rev. Cell Dev. Biol.* **27**, 731–758 (2011).
69. M. Martin, S. J. Iyadurai, A. Gassman, J. G. Gindhart Jr., T. S. Hays, W. M. Saxton, Cytoplasmic dynein, the dynactin complex, and kinesin are interdependent and essential for fast axonal transport. *Mol. Biol. Cell* **10**, 3717–3728 (1999).
70. R. G. Zhai, Y. Cao, P. R. Hiesinger, Y. Zhou, S. Q. Mehta, K. L. Schulze, P. Verstreken, H. J. Bellen, Drosophila NMNAT maintains neural integrity independent of its NAD synthesis activity. *PLOS Biol.* **4**, e416 (2006).

Acknowledgments: We thank L. Tang, H. Ji, and Y. Qiu for testing earlier versions of OptoTrap; D. Bank and Z. Zhong for writing the DendriteArborAnalyzer plugin; J.-Y. Tinevez for writing the DendriteDynamicTracker plugin; A. Nakamura (RIKEN Center for Developmental Biology) for Rbsn5 and Rab7 antibodies; Addgene for plasmids; Bloomington Stock Center for fly stocks; the Cornell Statistical Consulting Unit (CSCU) for aiding statistics analysis; and A. T. Lombardo for discussion and suggestions on the manuscript. **Funding:** This work was supported by the National Institutes of Health (grants R21OD023824, R01NS099125, and R24OD031953 to C.H. and grants R01NS102385 and R01NS116373 to J.W.). **Author contributions:** Conceptualization: C.H. and Y.X. Methodology: C.H., Y.X., B.W., and I.B. Reagents: Y.X., B.W., H.A.J.S., and J.W. Investigation: Y.X. Data analysis: Y.X., I.B., and C.H. Supervision: C.H. Writing—original draft: Y.X. and C.H. Writing—review and editing: C.H., Y.X., I.B., H.A.J.S., and J.W. **Competing interests:** The authors declare that they have no competing interests. **Data and materials availability:** All data needed to evaluate the conclusions in the paper are present in the paper and/or the Supplementary Materials. The code is available from Zenodo (doi:10.5281/zenodo.11585494).

Submitted 2 March 2024
Accepted 26 July 2024
Published 30 August 2024
10.1126/sciadv.adp0138